IAEA nuclear fusion

PAPER • OPEN ACCESS

Persistence of deuterium and tritium nuclear spin-polarization in presence of high-frequency plasma waves

To cite this article: J.W.S. Cook *et al* 2026 *Nucl. Fusion* **66** 056044

OPEN ACCESS
IOP Publishing | International Atomic Energy Agency Nuclear Fusion
Nucl. Fusion **66** (2026) 056044 (21pp) https://doi.org/10.1088/1741-4326/ae5ab8

Persistence of deuterium and tritium nuclear spin-polarization in presence of high-frequency plasma waves

J.W.S. Cook[1,2,3,*], **H. Ali**[4], **J.F. Parisi**[4], **A. Diallo**[5] and **N. Faatz**[6,7,8]

[1] Fourth State Labs Ltd, Culham Campus, Abingdon OX14 3DB, United Kingdom of Great Britain and Northern Ireland
[2] United Kingdom Atomic Energy Authority, Culham Campus, Abingdon, Oxfordshire OX14 3DB, United Kingdom of Great Britain and Northern Ireland
[3] Department of Physics, University of Warwick, Centre for Fusion, Space and Astrophysics, Coventry CV4 7AL, United Kingdom of Great Britain and Northern Ireland
[4] Marathon Fusion, 150 Mississippi, San Francisco, CA 94107, United States of America
[5] Princeton Plasma Physics Laboratory, Princeton University, Princeton, NJ, United States of America
[6] GSI, Helmholtzzentrum für Schwerionenforschung, Darmstadt, Germany
[7] III. Physikalisches Institut B, RWTH Aachen University, Aachen, Germany
[8] Institut für Kernphysik, Forschungszentrum Jülich, Jülich, Germany

E-mail: james.cook@ukaea.uk

Received 22 October 2025, revised 8 March 2026
Accepted for publication 2 April 2026
Published 30 April 2026

Abstract

We present first-principles numerical calculations of the depolarization rate of spin-polarized deuterium and tritium nuclei in realistic tokamak plasmas, driven by resonant interactions with plasma waves. Backed up by first-of-a-kind linear and nonlinear simulations, we find that alpha particle-driven Alfvénic modes cause only negligible depolarization, which is contrary to expectations in prior literature. Other Alfvénic instabilities can in principle degrade polarization, but only under conditions unlikely to be realized on transport timescales. By combining full-orbit particle tracing with a dedicated depolarization solver, we demonstrate that wave-driven depolarization is surprisingly weak in SPARC and ITER-scale devices. These results provide strong evidence that spin-polarized fuel can maintain its polarization long enough to boost fusion reactivity, opening a viable path toward substantially enhanced performance in magnetic confinement fusion power plants.

Keywords: spin polarized fuel, magnetized fusion plasmas, wave–particle interactions, fast ions, ion cyclotron emission, particle-in-cell

(Some figures may appear in colour only in the online journal)

---

[*] Author to whom any correspondence should be addressed.

1741-4326/26/056044+21$33.00 Printed in the UK

1. Introduction

For fusion power plants (FPPs) to become economically viable, they must sustain a sufficiently high volume-averaged fusion power density within the constraints of stability and engineering limits [1, 2]. Conventional strategies to raise power density rely on increasing plasma density and temperature through improved confinement, external heating, and optimized magnetic configurations [3–8].

An alternative and complementary strategy is to exploit the spin of the fuel nuclei. Polarizing the deuterium and tritium nuclear spins enhances the deuterium–tritium (D–T) fusion cross section [9–13], thereby boosting fusion power density without increasing plasma pressure [13–19]. This pathway is attractive because it bypasses stability and transport limits set by plasma pressure, heating and particle sources [20–35], while simultaneously increasing tritium burn-up and improving tritium self-sufficiency [36–38]. Spin polarization also modifies the angular distribution of fusion products [9, 11, 39–41], which could benefit tritium breeding, blanket transmutation, material longevity, and power conversion [42–44].

The promise of spin-polarized fuel (SPF) in FPPs is tempered by two key challenges: (i) ensuring that polarization survives long enough in the plasma to matter [11, 13, 39, 40], and (ii) developing SPF sources with sufficient throughput for reactor fueling [39, 45–47]. This work addresses the first challenge of polarization lifetime. In particular, we focus on depolarization by plasma waves—a mechanism whose severity remains uncertain but represents one of the largest barriers to SPF deployment.

Experimental data on spin survival in fusion-relevant conditions are limited. The only direct measurement to date, using accelerated ^{3}He ions, indicates that significant polarization can persist even at MeV energies [48]. This, together with extensive theoretical studies [9–11, 14, 49–53] and forthcoming experiments on the DIII-D tokamak [13, 39–41, 54], motivates computational exploration of depolarization in magnetically confined plasmas (MCF). While numerical studies exist for inertial confinement fusion [55, 56], no such work has yet been performed for MCF.

Depolarization in MCF plasmas may arise from many mechanisms including Coulomb collisions, wall interactions, or resonant wave–spin coupling. The first two mechanisms are generally benign under power plant conditions [11, 57–64]. The most concerning pathway is resonance between plasma waves and the nuclear magnetic moment [13]. In a magnetic field of strength B, nuclei precess at the Larmor frequency

$$\omega_L = \gamma_n B, \tag{1}$$

where γ_n is the nuclear gyromagnetic ratio. Plasma waves with frequency $\omega \approx \omega_L$ can resonantly drive spin flips [10, 11, 13, 39, 41, 49, 65, 66]. Alfvén waves, ion-cyclotron waves, and ion-Bernstein waves occupy this frequency range and may represent a significant threat to SPF survival [67–77].

In this paper we investigate cyclotron-frequency waves arising from several mechanisms including plasma normal modes, magnetoacoustic cyclotron instability (MCI), and compressional Alfvén eigenmodes (CAEs) [78–80]. Cyclotron-frequency waves due to ion cyclotron emission (ICE), arising from MCI [68, 78, 81–84] are ubiquitous in magnetized plasmas and have been found in nearly all large magnetically confined fusion devices: tokamaks including TFR [85], JET [86–91], TFTR [92–94], ASDEX-Upgrade [95–97], TUMAN-3 M [98, 99], DIII-D [100–102], EAST [103, 104], HL-2A [105, 106], JT-60U [107–112], KSTAR [113, 114], NSTX-U [115, 116]; stellarators including LHD [117, 118], W7-AS [119], W7-X [120]; and the linear machine, LAPD [121].

ICE typically occurs when an inverted distribution of fast ions resonates with the fast Alfvén wave at frequencies at or near successive ion cyclotron harmonics of the energetic species. This instability is known to be excited by so-called shells [83] of newly born alpha-particles as well as distributions comprising isolated regions of velocity space with well-defined parallel and perpendicular velocity, also known as ring-beams [122]. In tokamaks, these velocity space distributions typically occur in the edge where banana orbits take marginally trapped particles on large radial excursions to the outboard edge (see figure 8 of [93]), where they radiate so-called edge-ICE. Core-ICE can also be observed emanating from the tokamak core [96, 97, 106, 123]. ICE has also been reported from ohmic plasmas [98] providing evidence that some ICE signals may not be driven by fast ions. We show how polarized fuel gives rise to birth distributions of alpha-particles with more anisotropy than in the default unpolarized setting, and we go on to quantify any increase or decrease in growth rates of the MCI.

We investigate wave-induced depolarization in the infinite homogeneous plasma limit to establish a baseline physical understanding and present calculations for realistic tokamak geometries. Section 2 introduces SPF concepts and section 3 gives a simple picture of wave depolarization. Section 4 describes the equations used to study depolarization. Section 5 analyzes the plasma normal modes most relevant to resonant depolarization in the infinite homogeneous plasma limit, which partly informs the parameter space search for linearly unstable modes due to fusion product alpha-particles born from SPF ions, which are discussed in section 6. Fully kinetic nonlinear studies in the infinite homogeneous plasma limit by particle-in-cell (PIC) simulations in section 7 build upon the previous section provide an understanding of the characteristics of the fast-particle excited waves. Next, ensembles of particles are tracked in three dimensions in a SPARC-like geometry in section 8, providing some estimates of the potential capability of waves to depolarize fuel ions in an FPP. We conclude in section 9 with implications for the viability of SPF in future FPPs.

2. Spin-polarized fuel (SPF)

In this section, we describe SPF focusing on D–T fuel.

For a general D–T spin-polarization scheme, the differential D–T cross section depends on the pitch angle ϑ relative to the magnetic field $\mathbf{B}$ [11],

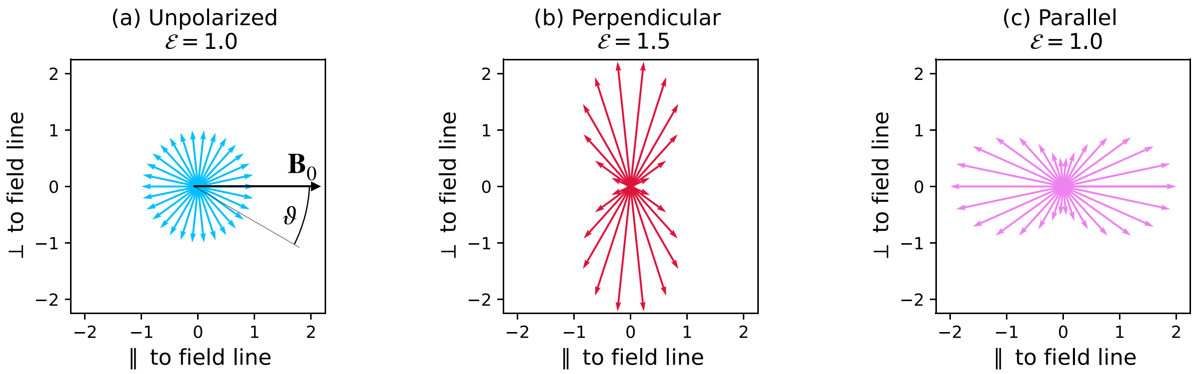

Figure 1. Relative density of neutron emission $F(\vartheta)$ (see equation (3)) parallel and perpendicular to the magnetic field $\mathbf{B}_0$ for three spin-polarization schemes: panel (*a*), unpolarized ($a = b = c = 0$); panel (*b*), perpendicular ($a = b = c = 1$); and panel (*c*), parallel ($a = b = 0, c = -2$). In (*a*) we indicate the pitch angle ϑ.

$$\frac{\mathrm{d}\sigma}{\mathrm{d}\Omega} = \frac{\sigma_0}{4\pi} F(\vartheta), \tag{2}$$

where σ_0 is the nominal unpolarized D–T cross section,

$$F(\vartheta) \equiv 1 - \frac{ab}{2} + \frac{1}{2}\left(3ab\sin^2\vartheta + \frac{c}{2}\left(1 - 3\cos^2\vartheta\right)\right), \tag{3}$$

and the polarizations are

$$\begin{aligned} a &= d_1 - d_{-1} \in [-1, 1], \\ b &= t_{1/2} - t_{-1/2} \in [-1, 1], \\ c &= d_1 + d_{-1} - 2d_0 = 1 - 3d_0 \in [-2, 1], \end{aligned} \tag{4}$$

where a and c are the deuterium vector and tensor polarizations, b is the tritium vector polarization, $d_m (m = -1, 0, 1)$ and $t_m (m = -1/2, 1/2)$ are the probabilities for deuterium and tritium to occupy a spin state m ($\sum_m d_m = \sum_m t_m = 1$), and the solid angle Ω is in Sterradians. The total cross section σ is modified by a factor $\mathcal{E}$,

$$\sigma = \frac{\sigma_0}{4\pi} \int_{\varphi=0}^{2\pi} \mathrm{d}\varphi \int_{\vartheta=0}^{\pi} F(\vartheta) \sin\vartheta \mathrm{d}\vartheta = \mathcal{E}\sigma_0, \tag{5}$$

where φ is the azimuthal angle. The polarization cross-section multiplier $\mathcal{E}$ is

$$\mathcal{E} \equiv 1 + ab/2, \tag{6}$$

and satisfies $\mathcal{E} \in [0.5, 1.5]$ [11]. Note that c affects $F(\vartheta)$ but never enters σ explicitly. Unpolarized fuel has $\mathcal{E} = 1$. A 50% cross-section enhancement ($\mathcal{E} = 1.5$) is obtained by choosing $ab = 1$ [11], corresponding to aligning the deuterium and tritium nuclear spins.

In figure 1 we plot $F(\vartheta)$, indicating the relative density of neutron emission parallel and perpendicular to the magnetic field, for three spin-polarization schemes: (*a*) unpolarized ($a = b = c = 0$), (*b*) perpendicular ($a = b = c = 1$), and (*c*) parallel ($a = b = 0, c = -2$). While the unpolarized scheme has isotropic neutron emission, the perpendicular scheme biases emitted neutrons perpendicular to the magnetic field and the parallel scheme biases parallel to the magnetic field. In this work, we will consider all three of these polarization schemes.

While the D–T fusion cross section is predicted to increase by as much as 50%, the corresponding power increase in MCF devices has been reported to be even higher. Recent work found that with $\mathcal{E} = 1.5$, the total fusion power increased by 80%–90% [13, 18] due to increased alpha heating. Similarly, in ICF the input energy requirement at constant gain is predicted to fall by nearly a factor of two [124].

3. Wave depolarization mechanism

In this section we describe how waves can depolarize nuclei. Nuclei with magnetic moments $\boldsymbol{\mu}$ and spin $\mathbf{I}$ in a magnetic field $\mathbf{B}(t)$ evolve according to

$$\begin{aligned} \frac{\mathrm{d}\mathbf{M}}{\mathrm{d}t} &= \gamma_n \mathbf{M} \times \mathbf{B}(t) - \frac{M_x\hat{\mathbf{x}} + M_y\hat{\mathbf{y}}}{T_2} \\ &\quad - \frac{\left(M_z - M_z^{\mathrm{eq}}\right)\hat{\mathbf{z}}}{T_1}, \end{aligned} \tag{7}$$

where $\mathbf{M} \equiv \langle \mu_n \mathbf{I} \rangle$ is the ensemble magnetization, M_z^{eq} is the equilibrium value of the longitudinal magnetization, and T_1, T_2 are the longitudinal and transverse relaxation times. The polarization is preserved, since all spins precess together. We decompose the total magnetic field into a time-independent equilibrium component $\mathbf{B}_0$ and time-dependent fluctuating component $\delta\mathbf{B}_\perp(t)$,

$$\mathbf{B} = \mathbf{B}_0 + \delta\mathbf{B}_\perp. \tag{8}$$

The fluctuating component $\delta\mathbf{B}_\perp$ describes a plasma wave whose electromagnetic fields include a small transverse, circularly polarized magnetic component,

$$\delta\mathbf{B}_\perp(t) = B_1 \left(\hat{\mathbf{x}} \cos\omega t + \hat{\mathbf{y}} \sin\omega t\right). \tag{9}$$

In the laboratory frame, this field rotates at frequency ω. In the rotating frame of the spin, if ω is sufficiently close to ω_L, the

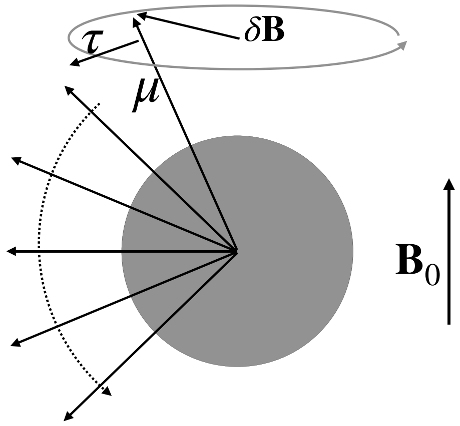

Figure 2. Schematic for how a circularly polarized wave with field $\delta\mathbf{B}$ exerts torque $\tau = \boldsymbol{\mu} \times \delta\mathbf{B}$ on a magnetic moment $\boldsymbol{\mu}$. If the wave and magnetic moment precession frequencies are close, there will be a torque for sufficiently long to change the component of $\mathbf{m}$ along the background field $\mathbf{B}_0$. Dashed arrow indicates the change of $\boldsymbol{\mu}$ over time.

wave's field appears nearly static and exerts a steady torque on the nuclear spin precessing at the Larmor frequency $\omega_L = \gamma_n B_0$. Physically, the wave is continuously 'nudging' the spin away from its original axis, just as in nuclear magnetic resonance. A conceptual representation of this process is shown in figure 2.

Each torque is tiny, because the spin's Zeeman energy $\mu_n B_0$ is only $\sim 10^{-7}$ eV in a Tesla-scale field, but resonance allows the nudges to accumulate coherently. Over time, the spin 'tips' away from its aligned orientation, and repeated events across the ensemble randomize the polarization.

Applying the rotating-wave approximation [125] to (7) in a frame rotating at ω shows that the spin precesses about an effective field

$$\mathbf{B}_{\text{eff}} = \frac{B_1}{2}\,\hat{\mathbf{x}} + \frac{\Delta}{\gamma_n}\,\hat{\mathbf{z}}, \qquad \Delta \equiv \omega_L - \omega, \tag{10}$$

with the Rabi frequency $\Omega_R = \gamma_n B_1/2$. On resonance ($\Delta = 0$), the spin is tipped at a rate Ω_R, so that after a characteristic time $\tau_R \sim \pi/\Omega_R$ the spin can be completely flipped. Including dephasing, the wave-induced depolarization rate per nucleus is

$$\Gamma_{\text{wave}} \;\approx\; \Omega_R^2 T_2 \;=\; \frac{\gamma_n^2 B_1^2}{4}\, T_2. \tag{11}$$

Thus even a very small transverse wave field B_1 can cause significant depolarization if T_2 is long.

Plasma waves are not usually coherent but form a spectrum. For a stochastic transverse field $B_+(t) = \delta B_x(t) + i\delta B_y(t)$ with spectral density $S_{B_+}(\omega)$, the spin-flip rate generalizes to

$$\Gamma_{\text{wave}} \;=\; \frac{\gamma_n^2}{2}\, S_{B_+}(\omega_L)\,. \tag{12}$$

Equation (12) states that depolarization occurs in proportion to the wave spectral power at the Larmor frequency, with the correct handedness. Physically, only those modes whose magnetic field rotates in close phase with the spin can continuously torque it; all others average away. Depolarization can thus be viewed as a resonance problem: the nuclear spin is a tiny 'antenna' tuned to ω_L, and any plasma wave with matching polarization and frequency can drive it. The survival of fuel polarization in a fusion plasma requires that

$$\Gamma_{\text{wave}}\, \tau_E \ll 1, \tag{13}$$

where τ_E is the confinement or fueling-replacement time. This condition highlights the challenge of maintaining nuclear spin polarization in the presence of waves: ensuring that the plasma spectrum has little power near ω_L.

4. Depolarization dynamics

In this section, we introduce the equations for studying depolarization of deuterium and tritium nuclei. This framework will form the foundation for inquiry in subsequent sections in configurations relevant to fusion machines.

The time-dependent Schrödinger equation describes the evolution of the deuterium or tritium wavefunction $\vec{\psi}$, which describes the evolution of nuclear spin,

$$\frac{\mathrm{d}\vec{\psi}}{\mathrm{d}t} = -\frac{i}{\hbar}\mathcal{H}\vec{\psi}, \tag{14}$$

where $\mathcal{H}$ is the Zeeman Hamiltonian. Electric dipoles of deuterons and tritons have not been measured and are not included. The Zeeman Hamiltonian is

$$\mathcal{H} = -g\mu_N \vec{B}_k S_{ijk} \tag{15}$$

where $g = 0.8574$ (5.9579) is the g-factor of the deuteron (triton), $\mu_N = 5.0509 \times 10^{-27}\,\mathrm{J\,T^{-1}}$ is the nuclear magneton, and $\vec{B}_k$ is the magnetic field vector and S_{ijk} is a spin tensor. Normalizing away factors of $\hbar$, the components of S_{ijk} for deuterium, and spin-1 particles in general, are

$$S_{ijx} = \begin{bmatrix} 0 & 1 & 0 \\ 1 & 0 & 1 \\ 0 & 1 & 0 \end{bmatrix} \frac{1}{\sqrt{2}}, \tag{16}$$

$$S_{ijy} = \begin{bmatrix} 0 & -i & 0 \\ i & 0 & -i \\ 0 & i & 0 \end{bmatrix} \frac{1}{\sqrt{2}}, \tag{17}$$

$$S_{ijz} = \begin{bmatrix} 1 & 0 & 0 \\ 0 & 0 & 0 \\ 0 & 0 & -1 \end{bmatrix}, \tag{18}$$

and the equivalent tensors for tritons (and spin 1/2 particles in general) are

$$S_{ijx} = \frac{1}{2}\begin{bmatrix} 0 & 1 \\ 1 & 0 \end{bmatrix}, \tag{19}$$

$$S_{ijy} = \frac{1}{2}\begin{bmatrix} 0 & -i \\ i & 0 \end{bmatrix}, \tag{20}$$

$$S_{ijz} = \frac{1}{2}\begin{bmatrix} 1 & 0 \\ 0 & -1 \end{bmatrix}. \tag{21}$$

The reference coordinate system for spin alignment is the z-axis, the direction of the static magnetic field $\vec{B}_0$.

The non-commutative nature of the operators [126] make it difficult to find analytical solutions to the spin Hamiltonian dynamics. They may only be found for limiting cases, such as for low field strengths, exact resonances or far from resonance. Magnus expansions [127] alleviate this problem but generate large and unwieldy expressions that retain these limitations to some extent. In this work, we choose to use a high-order ordinary differential equation solver which bypasses this problem and allows for the spin dynamics to be calculated simultaneously with charged particle motion in a magnetic field. For the remainder of this section we focus only on the spin dynamics of stationary particles.

The equation of motion of the spin Hamiltonian is integrated numerically using the 'Verner (9)8' [128] ordinary differential equation time-stepping algorithm with absolute and relative tolerances of 10^{-8}. The state vector of deuterium is a normalized 3-element complex vector $|\psi\rangle$,

$$|\psi\rangle = c_{-1}\,|-1\rangle + c_0\,|0\rangle + c_1\,|1\rangle, \tag{22}$$

where $|c_{-1}|^2 + |c_0|^2 + |c_1|^2 = 1$, and $|-1\rangle$, $|0\rangle$, and $|1\rangle$ are the basis vectors representing the instantaneous spin states $m_I \in [-1, 0, 1]$. In this work, we measure the spin states over time by calculating the instantaneous expectation values of $|\psi\rangle$ in the ith direction, $\langle\psi|\,S_i\,|\psi\rangle$, and (ii) the vector $\boldsymbol{\rho}$ of occupational probability of each spin state,

$$\boldsymbol{\rho} = \mathrm{diag}\left(|\psi\rangle\,\langle\psi|\right). \tag{23}$$

Figure 3 shows the time trace of ρ of these three states for a left handed magnetic perturbation with an amplitude 10^{-3} that of the bulk static field (electric field perturbations play no part and are not included). The deuteron is initially in the $m_I = 0$ state and the wave frequency is exactly the deuteron Larmor precession frequency. Over the course of 100 s of cyclotron periods, the deuteron depolarizes nearly completely to an average state of $\sim 1/3$ probability each, although the depolarization model features Rabi oscillations [129] whereby the spin states pass through their initial conditions.

When the frequency of the applied wave field moves further from resonance, the amplitude of the Rabi oscillations decreases but the frequency increases, as shown in figure 4.

There are two crucial observations to be made at this point: first, only relative magnetic perturbations perpendicular to the bulk magnetic field contribute to depolarization; second, only the left-handed component of the perpendicular magnetic perturbation can depolarize deuterons and tritons.

To investigate this further we perform scans of depolarization for left-handed magnetic field waves of varying amplitudes and frequencies. Figures 5(a) and (b) show how the temporal mean probability changes of a deuteron that is initially in the $m_I = 0$ state. They show that the resonance width of the depolarization process is narrower at lower amplitudes and that depolarization is negligible for relative wave amplitudes of 10^{-4}. Both the amount of depolarization and the width of the resonance increases with wave amplitude. Relative wave amplitudes of 10^{-2} are unlikely, but allow us to see the general trend of the structure of depolarization. We must understand the consequences of the increased anisotropy of SPF alpha-particles' birth distributions on the growth rates of waves in this range, which we investigate in later sections.

The inhomogeneous bulk magnetic field of a magnetized plasma FPP changes both the cyclotron frequency and Larmor precession frequency. As such, the spatial locations where a wave may resonantly depolarize a fuel ion are are localized,

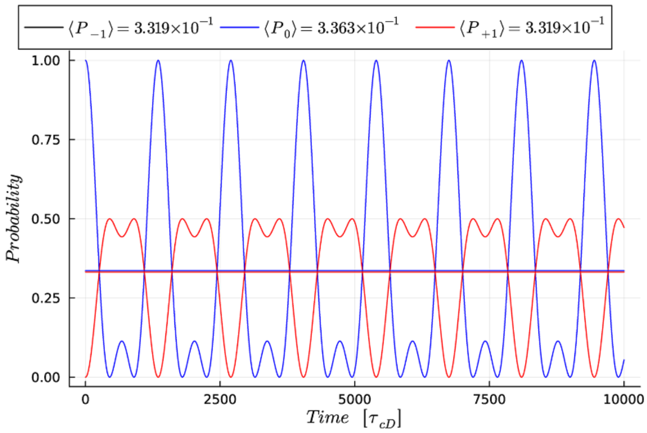

Figure 3. Time evolution of the probability density $\boldsymbol{\rho}$ (see equation (23)) of deuteron spin states over the course of 10 000 cyclotron periods in the presence of a left handed magnetic wave field with a frequency equal to the deuteron precession frequency and an amplitude $1/1000$ that of the bulk field. The curved traces represent the time evolution of the state probability and the straight lines show the temporal mean probability, values of which are listed in the legend.

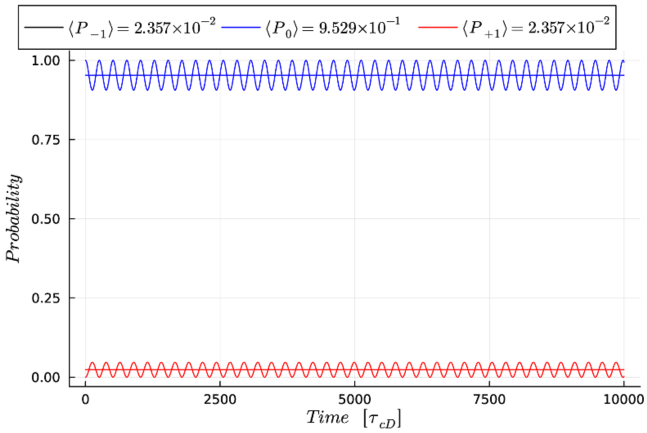

Figure 4. As in figure 3 except the wave field has a frequency 0.995 that of the the deuteron precession frequency.

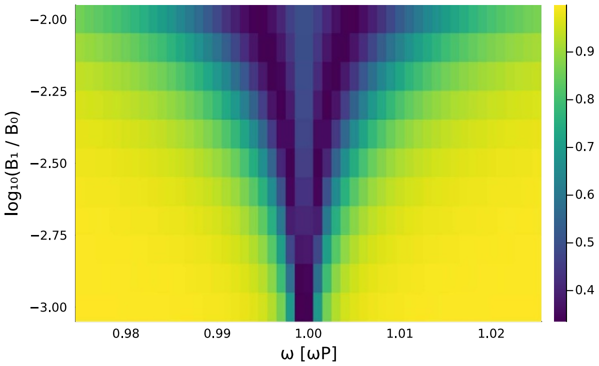

(a) The probability of finding a deuteron in spin state $m_I = 0$ after 10,000 cyclotron periods.

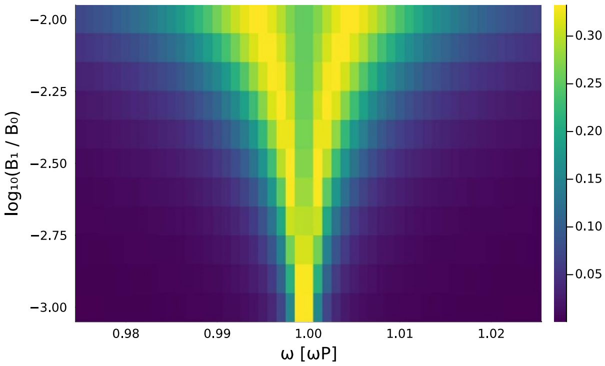

(b) The steady state probability of finding a deuteron in spin state $m_I = 1$ after 10,000 cyclotron periods. The result for $m_I = -1$ is identical.

Figure 5. Shading indicates the probability of finding a deuteron in a particular spin state after 10 000 cyclotron periods in the presence of a left-handed magnetic field wave with varying relative amplitudes and frequencies. The y-axis indicates the scan in relative amplitudes of wave field to bulk magnetic field on a $\log_{10}$ scale. The x-axis shows the frequencies in units of the deuteron Larmor precession frequencies. The deuteron is initially in $m_I = 0$. A probability of 1/3 for m_I indicates complete depolarization.

which for tokamaks are vertical stripes due to the $1/R$ dependence of the toroidal field. Particles must dwell within these regions in order to undergo coherent interactions leading to depolarization, hence only a subset of orbits are at risk.

In summary, we have introduced the formalism used for studying nuclear depolarization and demonstrated the effects of wave depolarization for several cases. We now proceed to study one of the mechanisms that leads to potentially depolarizing waves.

5. Normal modes

In this section, we study normal plasma modes that could depolarize D–T fuel. Normal modes of the plasma at frequencies near the deuterium and tritium precession frequencies are of particular interest. Focusing first on exploring them in the cold plasma limit, we find the dispersion surfaces of the waves that are supported by a 50–50 D–T mix plasma. From these surfaces we obtain the wave frequency and handedness with respect to the bulk magnetic field.

The quantity of interest of an arbitrary wave is the amplitude of the left-handed component. Stokes' parameters measure the polarization of an electromagnetic perturbation where $S_3 \in [-1, 1]$, when normalized by the amplitude S_0, and indicates the handedness where normalized $S_3 = +1$ is right-handed and normalized $S_3 = -1$ is left-handed. The relative amplitude of the perpendicular wave magnetic field is $|B_{1\perp}|/|B_1|$. Hence the product of these two quantities,

$$\frac{|B_{1\perp}|}{|B_1|}\left(1-\frac{S_3}{S_0}\right)\frac{1}{2}\in[0,1], \tag{24}$$

is indicative of the ability of a wave at or near resonance to depolarize a deuterons and tritons. Figure 6 introduces these quantities for the 3 normal modes near the deuteron and triton Larmor precession frequencies in a 50–50 DT mix plasma.

It is clear from the upper row of figure 6 that modes on the shear Alfvén branch do not reach the deuteron precession frequency and can be considered safe in terms of their capability to depolarize deuteron fuel. The intermediate mode, middle row, with small $|k_\perp|/|k|$ may depolarize deuterons while waves on the fast Alfvén branch, lower row, in the same wavenumber limit may depolarize both deuterons and tritons. Whether these modes are excited or not is another matter, which we turn to in the next section.

6. Fast-particle instabilities

In this section we investigate the degree to which alpha-particles born from different SPF schemes are unstable to the MCI and hence capable of causing ICE, which matters in this context for two very important reasons. The first reason is that it has the potential to emit waves at both the deuteron and triton Larmor precession frequencies, endangering the polarization of both species. The second reason is that polarization schemes alter the birth distribution of alpha-particles in pitch, resulting in greater anisotropy and therefore giving the distribution more free energy. In this section we quantify, for the first time, the difference in the MCI growth rates of alpha particles born from isotropically distributed fuel spins ($a = b = c = 0$) and that of the distribution function arising from parallel ($a = b = 0$, $c = -2$) and perpendicular ($a = b = c = 1$) schemes.

The pitch $p = \cos\vartheta$ of alpha-particles born from polarized D–T reactions can be drawn from 3 according the values of a, b, and c defined in equation (4) for the chosen SPF scheme. Unpolarized fuel ($a = b = c = 0$) results in isotropically distributed alpha particles on the surface of a sphere in three velocity space dimensions i.e. a shell distribution. The particles are all born with 3.5 MeV.

In the following numerical analysis we molify equation (3) by a Maxwellian thermal speed

$$f_{a,b,c}\left(v_z, v_\perp\right) \propto F\left(\vartheta\right)\exp\left(-\frac{\left(\sqrt{v_z^2+v_\perp^2}-v_0\right)^2}{v_{\mathrm{th}}^2}\right). \tag{25}$$

We find that the growth rate analysis remains largely unchanged when $v_{\mathrm{th}} = \frac{v_0}{100}$ or $\frac{v_0}{1000}$ (not shown), where v_0 is

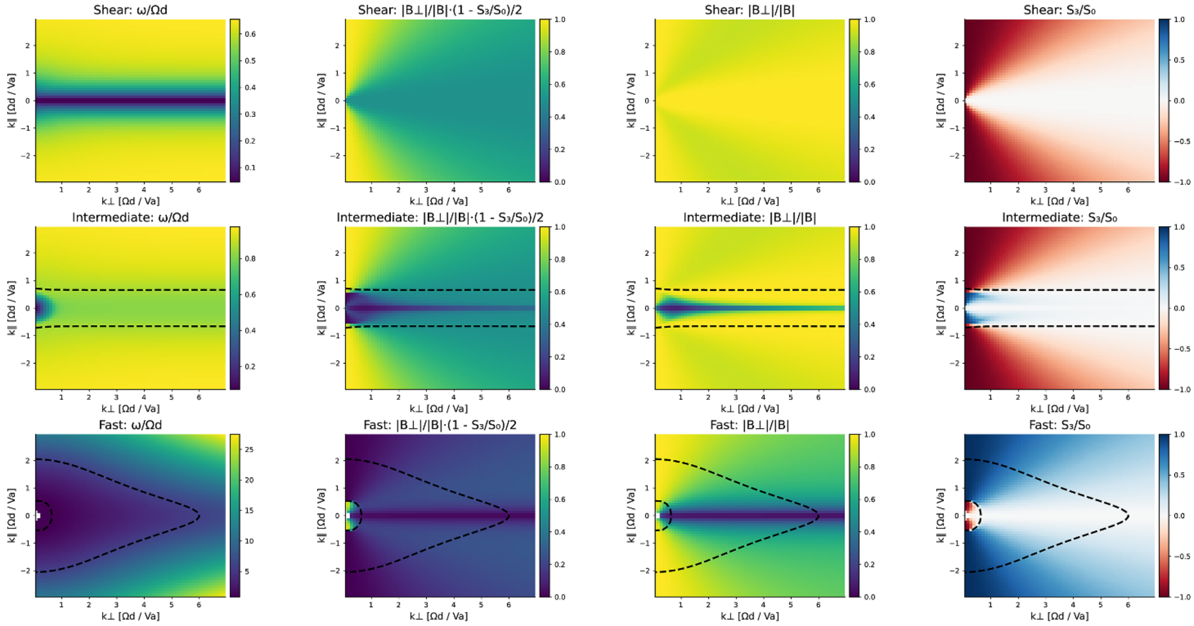

Figure 6. Normal modes of a 50–50 DT mix plasma in a parallel and perpendicular wavenumber plane. The three rows indicate three different normal modes of the system in order of lowest to highest frequency form top to bottom: the shear Alfvén wave; intermediate or hybrid mode; fast Alfvén wave. Shading of the four columns show different information about the normal modes, from left to right: frequency in units of the deuteron cyclotron frequency; the amount of perpendicular magnetic perturbation that is left handed, see equation (24); the relative fraction of perpendicular magnetic perturbation; the handedness of the wave, $+1$ (-1) is right (left) handed. The dashed black traces indicate frequency iso-contours at the deuteron and triton Larmor precession frequency, which are $\sim$0.86 and $\sim$5.9 respectively. The semi-circular black dashed linear in the lower right panel separates the red from blue region by chance—it does not do so for other DT ratios.

the speed corresponding to 3.5 MeV. v_{th} is intentionally small to ensure we destabilize waves that could pose a danger to the SPF ions.

The distribution function $f_{a,b,c}$ is passed into the linearized Maxwell–Vlasov set of equations [130–132], along with Maxwellian electrons, deuterons and tritons, in order to calculate its complex frequency solutions for sets of given $(k_z, k_\perp)$ pairs: see equations (5)–(9) of [84]. The linearized system describes the self-consistent growth or attenuation of electrostatic and electromagnetic wave oscillations that are supported by the collective motion of the individual plasma species. Maxwell's equations (26)–(29) determine the evolution of the electric field $\vec{E}$ and magnetic field $\vec{B}$, the Vlasov equation (30) and moments of the distribution function f_s of species s with charge q_s and mass m_s that provide the charge density ρ, equation (31), and current density $\vec{J}$, equation (32), as sources

$$\nabla \cdot \vec{B} = 0 \tag{26}$$

$$\nabla \cdot \vec{E} = \frac{\rho}{\epsilon_0} \tag{27}$$

$$\frac{\partial \vec{B}}{\partial t} = -\nabla \times \vec{E} \tag{28}$$

$$\mu_0 \epsilon_0 \frac{\partial \vec{E}}{\partial t} = \nabla \times \vec{B} - \mu_0 \vec{J} \tag{29}$$

$$\frac{\partial f_s}{\partial t} = -\vec{v} \cdot \nabla_x f_s - \frac{q_s}{m_s}\left(\vec{E} + \vec{v} \times \vec{B}\right) \cdot \nabla_v f \tag{30}$$

$$\rho = \sum_s q_s n_s \int \mathrm{d}v f_s \tag{31}$$

$$\vec{J} = \sum_s q_s n_s \int \mathrm{d}v \vec{v} f_s. \tag{32}$$

We use LinearMaxwellVlasov.jl [84, 133] to find these solutions after linearization. It makes efficient use of the Lerche–Newberger rules [132, 134, 135] to convert the standard truncated sum over cyclotron harmonics for integrals in $v_\parallel$ and $v_\perp$ into a single integral. Hence computationally tractable to find solutions in a two-dimensional $(k_z, k_\perp)$ plane.

The growth rates of the MCI are shown the following three figures 7–9 for the unpolarized, perpendicular and parallel SPF schemes, respectively. The color scale shows the growth rate in units of alpha-particle cyclotron frequency, and white indicates where the algorithm failed to find a solution, which in the upper right corners is where the damping rate is very strong, $\lesssim -0.015\Omega_i$. The x-axis (y-axis) is the parallel (perpendicular) wavenumber in units of Ω_D/V_A. Curved traces indicate contours of the real part of the complex frequency solution from which we obtain growth rates: the integers on the left and upper sides of the plot indicate the value of the real frequency in units of Ω_D. Straight dashed lines indicate angles of constant propagation in degrees off perpendicular, and solid lines

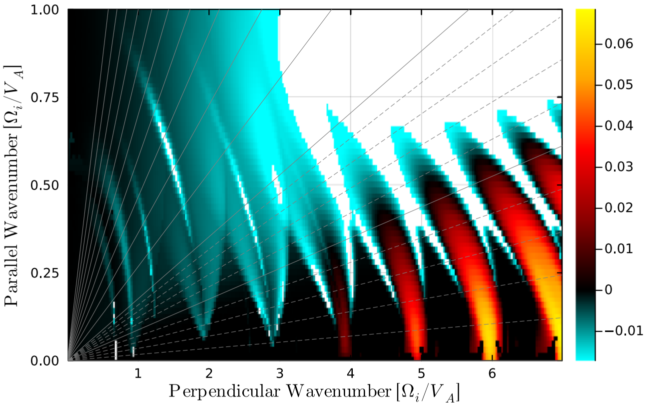

Figure 7. Shading indicates the growth rates of the unstable modes on the fast Alfvén dispersion surface on a two dimensional 128-by-128 parallel and perpendicular wavenumber grid. The unstable modes are driven by the anisotropic alpha-particle velocity space distribution, equation (25), born from spin-polarized DT reactions with spin parameters $a = b = c = 0$. Here $v_{\text{th}} = v_0/100$. The electrons and fuel deuterons and tritons are represented by Maxwellians with a temperature of 10 keV. White pixels in the figure indicate where the algorithm was not able to find a solution.

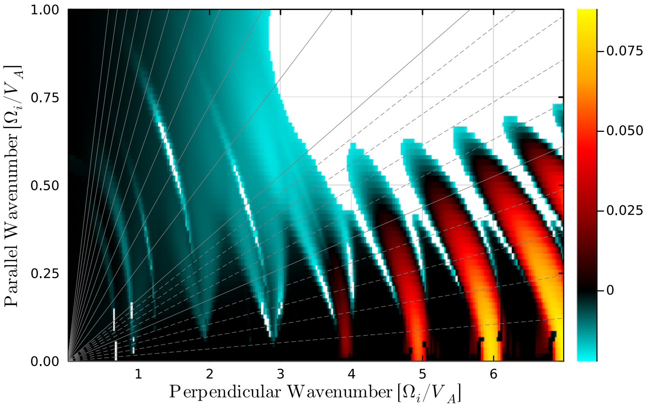

Figure 8. As in 7 except for the perpendicular SPF scheme ($a = b = c = 1$).

indicate the same in steps of 5 degrees. These plots are symmetric about $k_{||} = 0$ and only the upper half-plane in parallel wavenumber is plotted.

The perpendicular ($a = b = c = 1$) SPF scheme, shown in figure 8, generates growth rates that are approximate 20% larger than the unpolarized case. Finally, the parallel SPF scheme ($a = b = 0, c = -2$) in figure 9 shows the same mode structure with growth rates approximately $2/3$ that of the unpolarized case.

We see that for this background density of 10^{20} m^{-3} and magnetic field of 6 T, the unstable spectrum is located on and around the 4–7 alpha-particle cyclotron harmonics and that propagation is $\pm 6^o$ around perpendicular. Note that there is no instability at the deuteron Larmor precession frequency below the first cyclotron harmonic but the 6th harmonic, near the triton Larmor precession frequency, is unstable. However, referring to the cold-plasma dispersion surface in figure 6, we see that these waves have very little left-handed perpendicular perturbations making them benign in terms of their ability to depolarize the fuel.

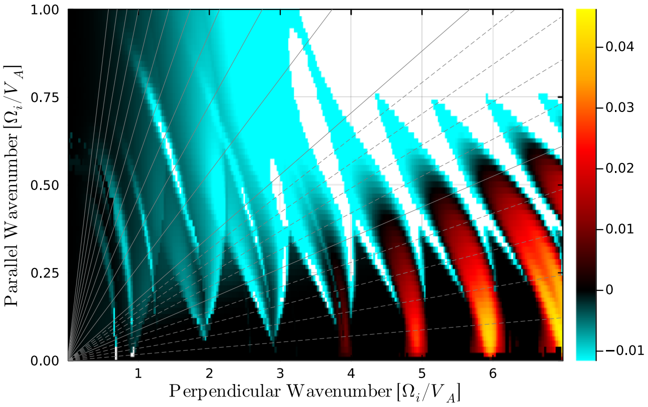

Figure 9. As in 7 except for the parallel SPF scheme ($a = b = 0$, $c = -2$).

Given that ICE is not regularly observed from unpolarized fuel alpha-particles before they have slowed down, this suggests that ICE from fuel polarized alpha-particles will not present a massive threat given their growth rates are broadly similar.

Non-linear interactions between ICE waves at adjacent higher harmonics couple power to the lower harmonics, including the fundamental [121, 136]. This could be a mechanism where ICE power is cascaded down to the deuteron Larmor precession frequency where the left-handed perpendicular magnetic perturbation is no longer negligible.

7. PIC simulations

In this section, we describe PIC [137, 138] simulations of SPF fusion born alpha-particle driven instabilities in fusion plasma conditions. PIC has been used to model the MCI associated with energetic ion distributions where, importantly, it takes the physics into the nonlinear phase allowing power emitted from linearly unstable high harmonics to couple to lower harmonics [121–123, 139–143]: it is this coupling that offers an extra energy transfer channel from fast ions to waves at and near the Larmor precession frequencies of the fuel ions. These fully nonlinear self-consistent simulations provide an estimate of the amplitude of these waves, which informs the analysis of the next section.

Introducing SPF in fusion reactors results in an anisotropic distribution of fusion products which can excite distinct magnetic perturbations in a plasma. Here we use the PIC code, EPOCH [144], in one spatial dimensions to self-consistently evolve Maxwell's equations and particles with three velocity components under the Lorentz force. We estimate the size of magnetic perturbations driven by the anisotropic alpha particle distribution in a spin-polarized 50–50 D–T plasma. The standard EPOCH source code is modified to incorporate the initial alpha particle distribution function corresponding to various values of a, b, and c, as described in equations (4) and (3).

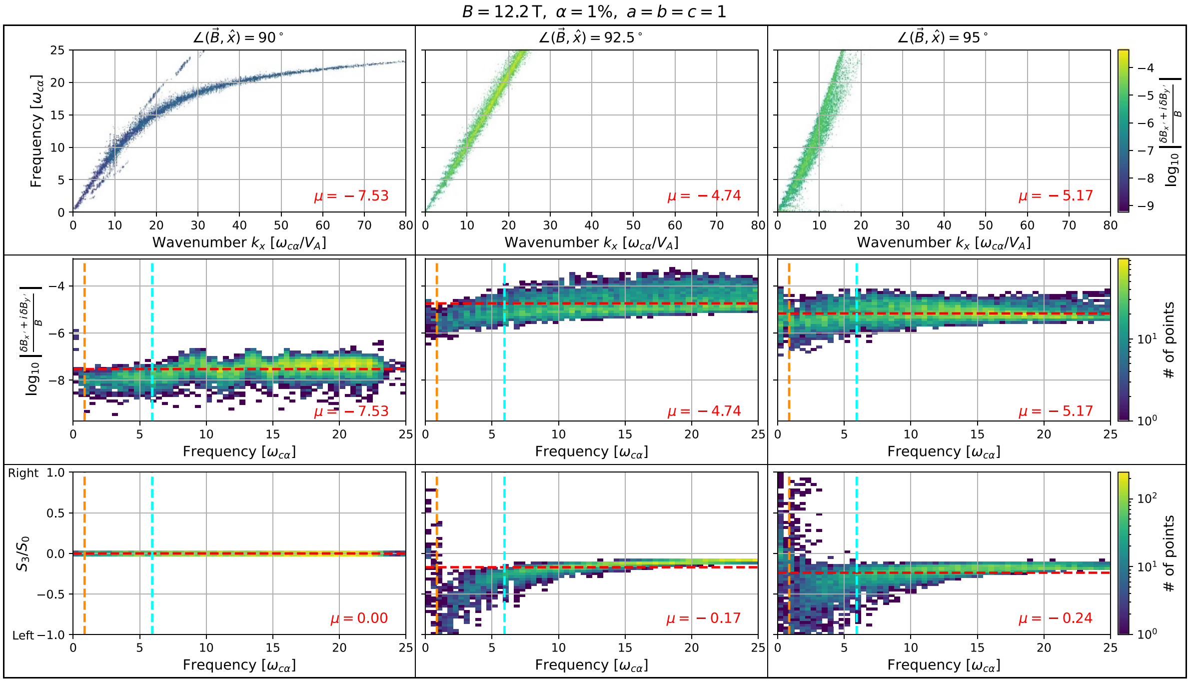

Figure 10. EPOCH simulation results for SPARC conditions at three magnetic field orientations relative to the simulation domain ($\angle(\vec{B},\hat{x}) = 90°, 92.5°, 95°$, shown column-wise), with constant alpha fraction ($\alpha = 1\%$) and perpendicular fuel polarization ($a = b = c = 1$). Color in the top row shows the $\log_{10}$ of the absolute value of the circular polarization component of the magnetic field waves, normalized to the bulk magnetic field, as a function of frequency against wavenumber. The middle row shows two-dimensional histograms of the data plotted in the upper panels as a function of the magnitude of the circular polarization component of the magnetic wave fields against frequency. The lower panels are similar to the middle panels except the ordinate is the handedness Stokes parameter of the waves. The orange and cyan vertical dashed lines indicate the deuteron and triton Larmor precession frequencies, respectively. On all plots μ shows the mean value of the quantity plotted in each panel.

Each simulation is evolved for a duration of eight alpha cyclotron periods. The single spatial axis is aligned along the x-axis whilst the background magnetic field $\mathbf{B}$ has a fixed magnitude and lies in the x–z plane. The direction of $\mathbf{B}$ relative to the x-axis, fuel polarization (a,b,c), and alpha fraction (α) are varied across simulations. The simulations are run for SPARC ($T = 7\,\mathrm{keV}$, $n = 3\times10^{20}\,\mathrm{m}^{-3}$, $B = 12.2\,\mathrm{T}$) and ITER ($T = 15\,\mathrm{keV}$, $n = 1\times10^{20}\,\mathrm{m}^{-3}$, $B = 5.3\,\mathrm{T}$), where T and n are the plasma temperature and density respectively.

Magnetic field fluctuations transverse to $\mathbf{B}$ can be expressed as the superposition of left-hand and right-hand circularly polarized components, defined relative to an axis parallel to $\mathbf{B}$. Depolarization takes place only when the wave rotates in the same direction as the ion is precessing. The left-hand component is of particular importance as it can interact resonantly with nuclear spin precession; a frequency match between the two provides a direct channel for spin depolarization. We obtain these magnetic field wave characteristics from EPOCH simulations as a function of frequency and wavenumber via Fourier transform. The wavenumber k is defined by the axis of variation in EPOCH, i.e. the x-axis. Through the parameter scan in angle between the magnetic field and the x-axis, the plane perpendicular to the magnetic field changes and hence a rotation around the y-axis is deployed to obtain the wave information in a coordinate system $(x', y' = y, z')$ where the magnetic field points exactly along z'. This ensures consistent extraction of perpendicular magnetic fluctuations $\delta B_{x'}$ and $\delta B_{y'}$, from which the relative left-hand component $|(\delta B_{x'} + i\delta B_{y'})/B|$, as well as the Stokes ratio $S_3/S_0 = -2\,\mathrm{Im}(\delta B_{x'}\,\delta B^{\dagger}_{y'})\,/\,(|\delta B_{x'}|^2 + |\delta B_{y'}|^2)$, are subsequently calculated.

The simulation results are presented for the SPARC [5], see figures 10–12) and ITER (appendix) tokamaks. The frequency and wavenumber axes are normalized to the alpha cyclotron frequency, $\omega_{c\alpha}$, and $\omega_{c\alpha}/V_\mathrm{A}$, respectively, where V_A is the Alfvén speed. For each subplot, the mean value (μ) of the relevant quantity is indicated by a horizontal red dashed line and annotated with red text. Vertical dashed lines mark the precession frequencies of deuterium (orange) and tritium (cyan), which occur at approximately $0.86\omega_{c\alpha}$ and $5.94\omega_{c\alpha}$, respectively [11].

Based on all the simulation results, it can be seen that the primary magnetic field fluctuations in the (ω, k) spectra correspond to the fast Alfvén branch, with superposed discrete ion-cyclotron resonances. This result indicates that Alfvén waves, rather than ion-cyclotron instabilities, constitute the dominant threat to sustaining spin polarization. In figure 10, as the angle $\angle(\vec{B},\hat{x})$ shifts from perpendicular to slightly oblique (92.5° and 95°), the emergence of a non-zero parallel wavenumber $(k_\parallel)$ increases the mean magnetic field fluctuations amplitude by two to three orders of magnitude and drives a transition from linear to left-handed polarization. At oblique angles, the wave polarization transitions from left-handed $(S_3/S_0 < 0)$ at low frequencies to nearly linear $(S_3/S_0 \approx 0)$ at higher frequencies,

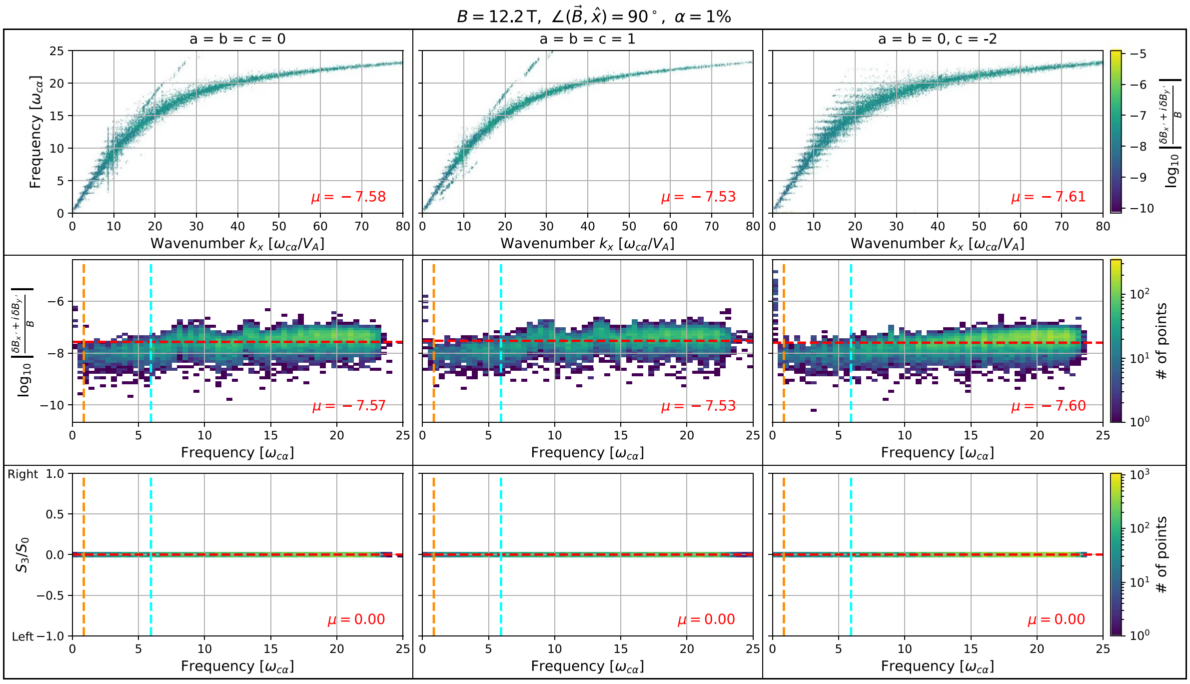

Figure 11. EPOCH simulation results for SPARC conditions at three fuel polarization configurations (unpolarized $a = b = c = 0$, perpendicular $a = b = c = 1$, and parallel $a = b = 0$, $c = -2$, shown column-wise), with constant magnetic field orientation $\angle(\vec{B}, \hat{x}) = 90°$, and alpha fraction $\alpha = 1\%$.

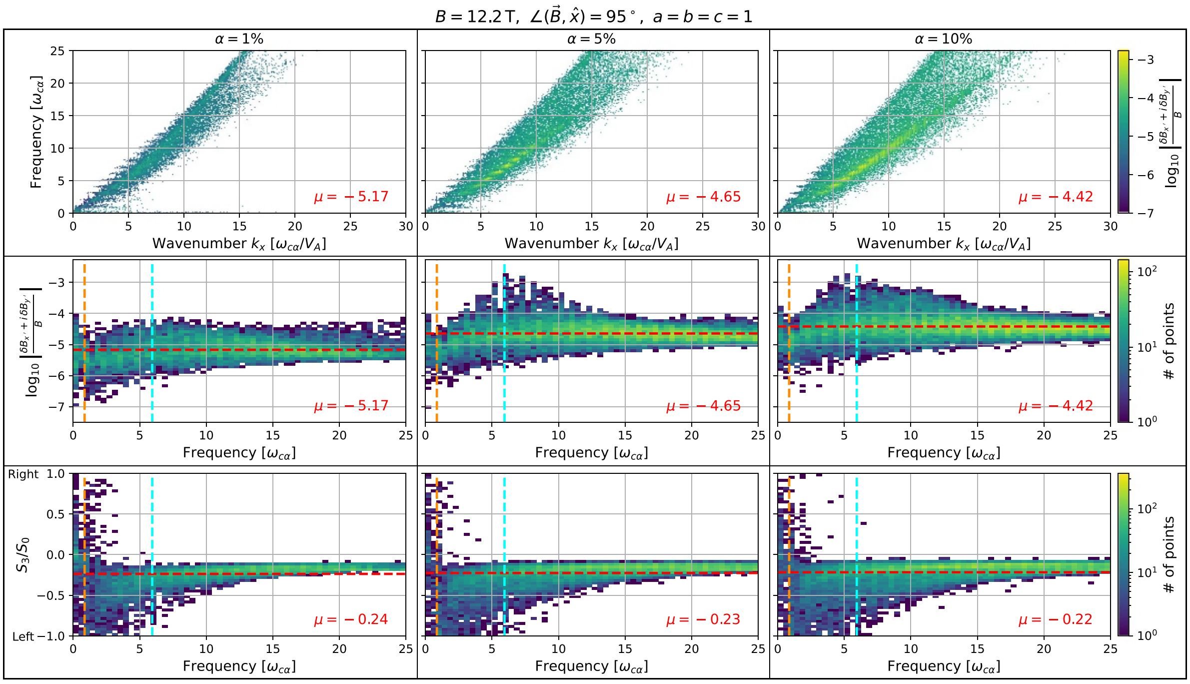

Figure 12. EPOCH simulation results for SPARC conditions at three alpha fractions ($\alpha = 1\%, 5\%, 10\%$, shown column-wise), with constant magnetic field orientation $\angle(\vec{B}, \hat{x}) = 95°$, and fuel polarization $a = b = c = 1$.

in contrast to the purely linear polarization observed at 90°.

The magnetic fluctuation amplitude is largely insensitive to the choice of fuel polarization (a, b, c), with both the amplitude spectra and the Stokes parameter ratio S_3/S_0 remain nearly unchanged across all polarization schemes, as illustrated in figure 11. Increasing the fast-alpha fraction from $\alpha = 1\% \rightarrow 5\% \rightarrow 10\%$ raises the mean level from $\mu = -5.17 \rightarrow -4.65 \rightarrow -4.42$, while the mean polarization (S_3/S_0) remains weakly left-handed and nearly propagation angle independent as shown in figure 12. Similar results are also obtained for ITER (appendix).

8. Particle tracking in realistic geometry

In this section, we integrate our spin-depolarization code with realistic particle trajectories in a realistic geometry.

One may integrate several trajectories originating from across phase space and perform a Monte Carlo integral of the bulk expected depolarization state $<\bar{\psi}_0>$ over an evolution time τ, where

$$\langle\bar{\psi}_0\rangle = \frac{\sum_{v_\parallel}\sum_{v_\perp}\sum_V \bar{\psi}_0\left(v_\parallel, v_\perp, V\right) v_\perp \Delta V \Delta v_\parallel \Delta v_\perp}{\sum_{v_\parallel}\sum_{v_\perp}\sum_V v_\perp \Delta V \Delta v_\parallel \Delta v_\perp}. \tag{33}$$

Figure 13 displays a convergence study for such a calculation on a SPARC-like machine, beginning with all particles in the $m_I = 0$ state in the presence of a left-handed wave with zero wavenumber (to deliberately exclude Doppler-shift enabled resonances) and amplitude 10^{-3} that of the field on axis. The wave frequency is that of the precession frequency on-axis. Deuterons are drawn uniformly from temperatures on-axis of 0.1, 1 and 10 keV, which fall off quadratically in $s = \sqrt{1 - \psi/\psi_{\mathrm{ax}}}$ towards the last closed flux surface (LCFS), where ψ is the poloidal magnetic flux and ψ_{ax} is that on axis. A resolution study has been performed in the linear scan size N, where N is the number of equally spaced samples in the integration dimensions; flux surfaces, parallel velocity and perpendicular velocity. The particles are tracked for 10 000 on-axis cyclotron periods. Initially, the deuterons are all in the $m_I = 0$ state and we see that the temporal mean state sees a reduction of depolarization by ~3.5%. The other two states split the remaining probability equally between them.

One would need to run these with high values of N for more accurate results and include collisions to allow particles to traverse phase space whilst going into and out of resonance. The next subsection accounts for non-zero wavenumber and multiple co-existing waves.

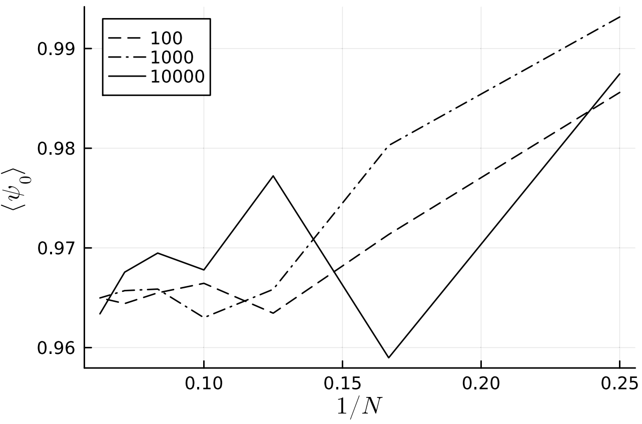

Figure 13. The spatio-temporal expectation value of the $m_I = 0$ state, initially fully occupied, evaluated from an ensemble of particles integrated over 10 000 cyclotron periods (as calculated on axis) for a SPARC-like equilibrium. The dashed, dot-dashed and solid traces indicate estimates for plasmas of 100, 1000 and 10 000 eV, respectively. Here N is the number of locations in minor radius, parallel velocity and perpendicular speed at which particles are initialized in order to perform the Monte-Carlo integral of spatio-temporal expectation spin state.

Bulk spin depolarization by eigenmodes in SPARC

The bulk spin depolarization of an ensemble of initially polarized deuterium or tritium ions is evaluated in the SPARC axisymmetric equilibrium magnetic field—modeled using a Solov'ev equilibrium with Miller shaping (major radius $R_0 = 1.85$m, on-axis toroidal field $B_0 = 12.2$ T, inverse aspect ratio $\epsilon = 0.31$, elongation $\kappa = 1.97$, and triangularity $\delta = 0.54$)—in the presence of superimposed eigenmode perturbations. Inspiration from CAE-like structures [78–80] is drawn from the active area of study on the link between higher frequency MCI fast Alfvén modes that give good agreement from infinite homogeneous plasma models and the geometry dependent cyclotron and sub-cyclotron eigenmodes of Hall-MHD [145–148]. However unlike CAEs, we ensure that the magnetic perturbation of our hypothetical eigenmode has a significant shear component to maximally endanger polarization (the perturbed magnetic field orthogonal to the bulk magnetic field is at least $\simeq 75\%$). The plasma volume is radially discretized into $N_v = 10$ approximately equal-volume nested toroidal shells, $\{\Delta V_i\}_{i=1}^{N_v}$, representing the volume between adjacent magnetic flux surfaces fixed by the normalized minor-radius coordinate $s_i = \sqrt{1 - \psi_i/\psi_{\mathrm{ax}}}$, where ψ_i is the poloidal flux on the ith surface and ψ_{ax} is its value at the magnetic axis, such that $s = 0$ at the axis and $s = 1$ at the LCFS. Ions are initialized on the outboard midplane of each flux surface s_i at major radius R_i. At each of these spatial locations, the velocity space is sampled on a tensor grid of $N_E \times N_E$ points (where $N_E = 10$) in parallel and perpendicular kinetic energy relative to the equilibrium magnetic field, $(E_{\parallel,j}, E_{\perp,k})$. The grid points are quadratically spaced from 0 to $E_{\max} = 100\,\mathrm{keV}$ (10 times that of the characteristic temperature) according to the relation $E_n = E_{\max} u_n^2$, where $\{u_n\}_{n=1}^{N_E}$ is drawn from a uniform distribution in $[0, 1]$. This non-uniform sampling provides a higher density of grid points at low energies, which better represents the bulk of a thermal Maxwellian distribution while sparsely sampling the high-energy tail. For each discrete initial condition (position R_i and energy $\{E_{\parallel,j}, E_{\perp,k}\}$), the evolution of a single spin polarized ion is simulated on collisionless timescales. The particle's trajectory is determined by the Lorentz force, while its spin state, $|\psi(t)\rangle$, evolves according to the time-dependent Schrödinger equation, yielding the probability of the ion being in each specific spin state m_I as a function of time $P_{m_I,ijk}(t)$. The final bulk probability is then determined by scaling this $P_{m_I,ijk}(t)$, by a weighting factor, W_{ijk}, calculated as follows to represent its statistical significance within the overall particle distribution

$$W_{ijk} = \left(1 - s_i^2\right) e^{-\frac{E_{\parallel,j}}{T}} e^{-\frac{E_{\perp,k}}{T}} \sqrt{E_{\perp,k}} \Delta V_i. \tag{34}$$

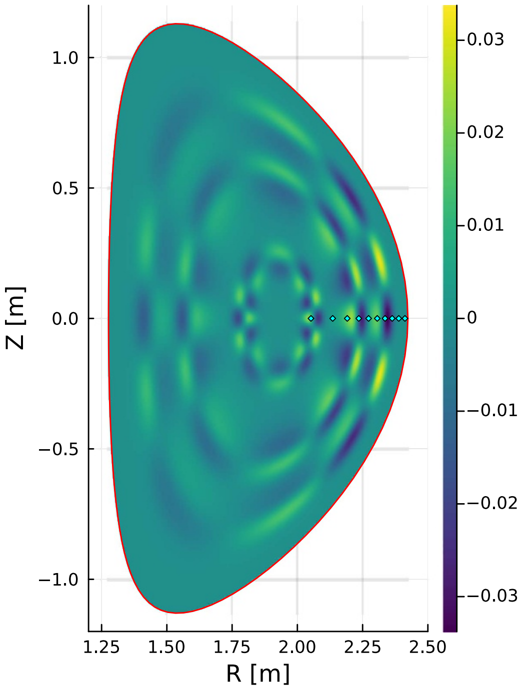

Figure 14. Poloidal magnetic field component of eigenmode perturbations in the SPARC tokamak plasma at $t = 0$, shown in the (R, Z) cross-sectional plane. The structure is superposition of three eigenmodes, each of which has the amplitude 3×10^{-3} of the magnetic field strength on axis. The red line indicate the plasma boundary, and the cyan diamonds mark the initial positions of ions on the outboard midplane. Color indicates field strength in Tesla.

Here $(1 - s_i^2)$ provides a parabolic on-axis-peaked density profile, the Maxwellian factors $\exp(-E/T)$ weight the energy grid at a common temperature $T = 10\,\mathrm{keV}$ (identical in $\|$ and $\perp$), a term from the velocity-space volume element, $v_{\perp,k} \propto \sqrt{E_{\perp,k}}$, and ΔV_i converts the surface sum into a volume integral. The final bulk probability for a specific spin state m_I as a function of time, $\langle P_{m_I}(t)\rangle$, is given by the weighted average over the entire simulated particle distribution:

$$\langle P_{m_I}(t)\rangle = \frac{\sum_{i,j,k} P_{m_I,ijk}(t) \cdot W_{ijk}}{\sum_{i,j,k} W_{ijk}}. \tag{35}$$

This summation is the numerical approximation of the continuous integral over the ions' phase-space distribution function.

To estimate fuel ion depolarization, we consider a representative example of eigenmode-like magnetic perturbations, noting that the resulting depolarization depends on the assumed perturbation structure, localization, frequency and amplitude. Eigenmode perturbations at a given position and time (see figure 14) are modeled as a superposition of three eigenmodes, expressed via magnetic fluctuations of the form $\nabla \times (\alpha \vec{B}_0)$, where:

$$\alpha \propto \Re\left[\sum_{l=1}^{3} \nabla \times \left(e^{i\Phi_l} e^{-\frac{(s-s_l)^2}{\Delta s^2}}\right)\right] \tag{36}$$

and the phase of the lth mode $\Phi_l = m_l\theta - n_l\phi - \omega_l t$, with $m_l = 6$ and $n_l = 3$ denoting the poloidal and toroidal mode numbers, respectively. The selected wave structure (m_l, n_l) is consistent with the symmetry of low-toroidal-mode-number Alfvénic and energetic-particle-driven instabilities commonly observed in tokamaks. Each mode's angular frequency ω_l is set to the deuteron or triton precession frequency evaluated at s_l indicated by the 1st, 4th and 7th dots in figure 14, counting outwards. Modes are localized to flux surfaces by a Gaussian radial envelope centered on s_l with a width of $\Delta s_l = 0.05$. The modes are scaled such that spatially $\max\left(|\delta B^l|\right) = 3 \times 10^{-3}|B_{0,\mathrm{axis}}|$. The chosen amplitude level reflects the highest order-of-magnitude magnetic fluctuation obtained in the PIC simulations presented in the previous section, and is therefore intended as an upper-bound estimate of the perturbation strength.

Figures 15 and 16 show that for deuterium with different initial spin polarizations relax to a quasi-steady state after approximately 0.03 ms. Deuterium starting in the $m_I = +1$ state retains an average probability of 0.8905, compared to an initial $m_I = 0$ state, which averages a probability of 0.8628. A difference appears in how the other states are populated: when starting from $m_I = 0$, the $m_I = +1$ and $m_I = -1$ states are populated equally. However, when starting from $m_I = +1$, the $m_I = 0$ state is populated more than the $m_I = -1$ state. This asymmetry stems from the quantum mechanical selection rules for magnetic dipole transitions, which only allow spin transitions of $\Delta m_I = \pm 1$. As a result, a direct transition from $m_I = +1$ to $m_I = -1$ is forbidden, forcing the spin to

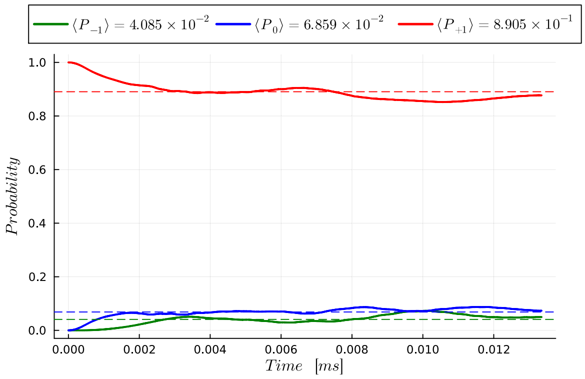

Figure 15. Time evolution of the bulk probability density of deuterons spin states in SPARC, initialized in the spin polarized state $m_I = 1$, on collisionless timescales in the presence of eigenmode perturbations. The thick curved traces represent the time evolution of the spin state probability, while thin straight lines indicate their temporal mean values, listed in the legend.

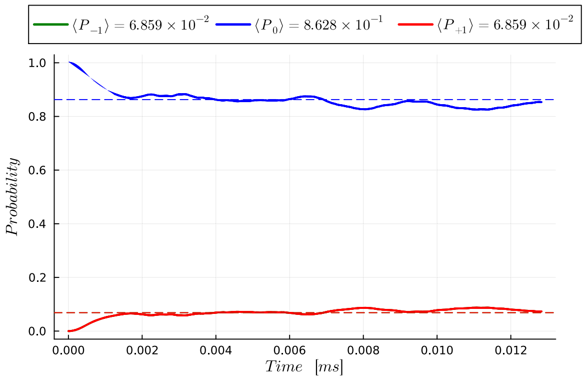

Figure 16. As in figure 15 except deuterons are initialized in the spin polarized state $m_I = 0$.

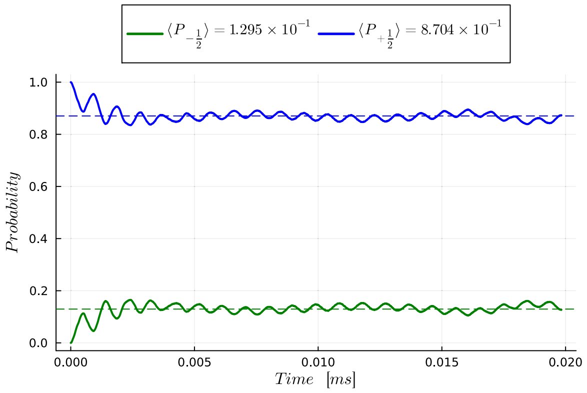

Figure 17. As in figure 15 except tritons are initialized in the spin polarized state $m_I = +1/2$.

pass through the intermediate $m_I = 0$ state—leading to its enhanced population while the $m_I = -1$ state remains suppressed. Results for tritium (see figure 17) show ~13% depolarization. Overall, both tritium and deuterium exhibit a measurable depolarization of $\simeq 12 \pm 1\%$ in SPARC for these strong eigenmode perturbations over collisionless timescales. Results show that there is no measurable depolarization for the same simulations where the eigenmode frequencies are changed to the precession frequency of the other ion species; i.e. deuterons remain polarized in waves tuned to the triton precession frequency and vice versa.

Although bulk spin depolarization provides an overall estimate, it is also important to investigate the depolarization of individual ions in SPARC to better understand the underlying physics at the particle level. A resonant interaction between a wave and a moving spin-polarized nucleus occurs when the wave's frequency, ω, satisfies the condition:

$$\omega = \omega_L + \ell\omega_c + k_{\|}v_{\|}.$$

Here, ω_L is the Larmor frequency, ω_c is the cyclotron frequency, $k_{\|}v_{\|}$ is the Doppler shift (calculated from the wave's parallel wavenumber, $k_{\|}$, and the nucleus's parallel velocity, $v_{\|}$), and ℓ is the integer cyclotron harmonic number [11]. Modeling reveals that depolarization is confined to a narrow Doppler-shifted band around the fundamental Larmor resonance ($\ell = 0$) with negligible coupling to cyclotron harmonics. For this reason, depolarization is examined exclusively at the fundamental resonance. This is an encouraging result, as it means that only a single frequency band around the precession frequency can cause depolarization, while all higher harmonics remain benign. It is also important to note that in cases where multiple waves resonate with the spin polarized nucleus at a given location, the net magnetic perturbation amplitude, δB, is determined by the superposition of the waves. The outcome of this superposition depends on the individual wave parameters as described by equation (36), which dictate the critical relative phases between them. Generally, constructive interference between waves increases the effective perturbation amplitude and thereby enhances depolarization, whereas destructive interference reduces the net amplitude, potentially canceling the perturbations and preserving polarization.

To study the dependence of depolarization on particle energies, a deuteron in the spin-1 state is launched from the outboard mid plane at selected R_i with prescribed parallel and perpendicular energies ($E_{\|}$, $E_{\perp}$) in SPARC. The wave frequency ω is set to the local deuteron precession frequency, evaluated from the equilibrium magnetic field B_{res} at R_i, with $\boldsymbol{\delta B} = [B_{\mathrm{res}}/1000, 0, 0]$ and $k = 0$, so that Doppler-shift effects are neglected. Particles are classified as passing or trapped based on their pitch angle, $\xi = \tan^{-1}\left(\sqrt{E_{\|}/E_{\perp}}\right)$, with passing particles satisfying $\tan^{-1}(\sqrt{2\epsilon}) < \xi < \pi/2$ and trapped particles satisfying $0 < \xi < \tan^{-1}(\sqrt{2\epsilon})$. Here, $\epsilon = r/R$ is the inverse aspect ratio of the flux surface at the particle's initial position, with r the minor radius and R the major radius. Each simulation is run over 10^4 cyclotron periods (collisionless timescales), and the resulting mean temporal probability is evaluated as shown in figure 18. In addition, figure 19, also shows example trajectories for a trapped particle (inner banana orbit) and a passing particle (outer circular orbit), where color indicates the instantaneous probability

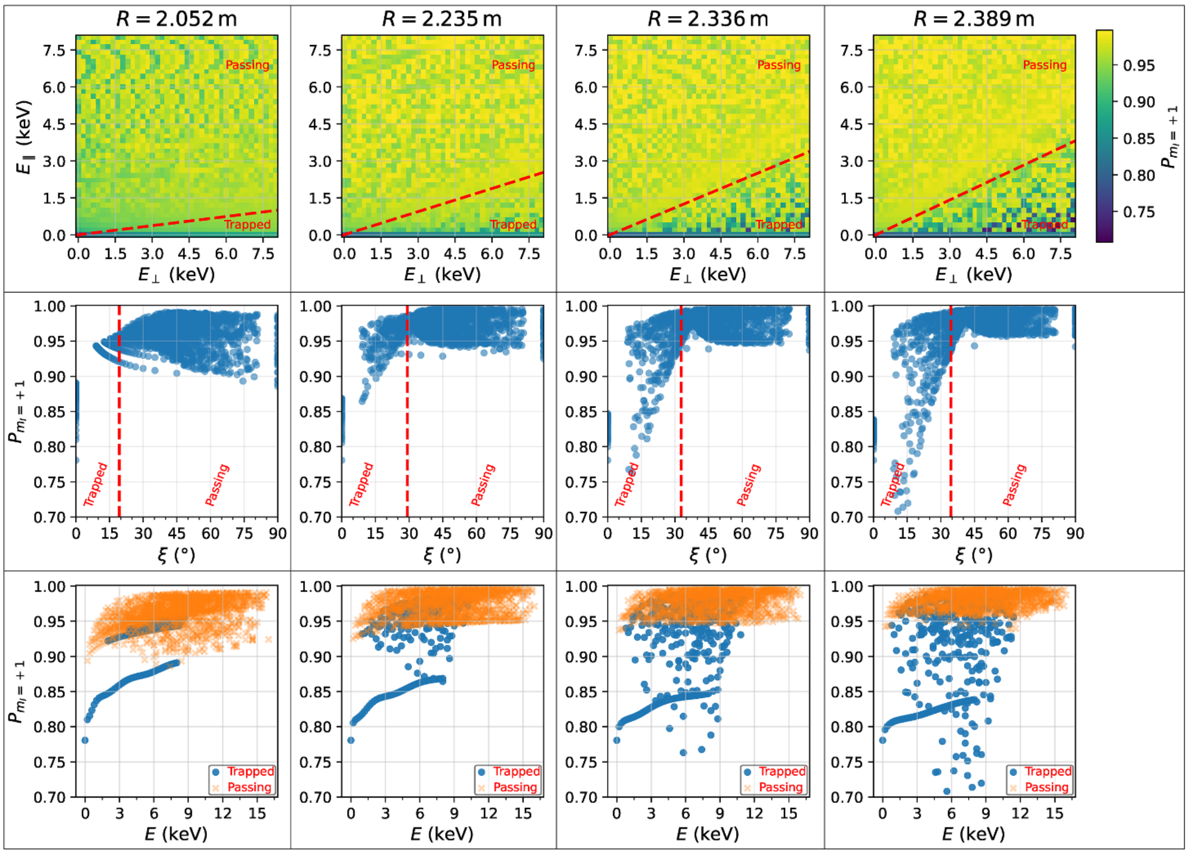

Figure 18. Mean temporal probability of a deuteron in the $m_I = +1$ state, averaged over 10^4 cyclotron periods in SPARC, shown across $(E_\parallel, E_\perp)$ space (top row), pitch angle (middle row), and total energy (bottom row), with red dashed lines marking the trapped-passing boundary. Each column corresponds to a different major radius R_i on the outboard midplane where deuterons are initialized. The wave frequency is set to the local deuteron precession frequency, evaluated from the equilibrium magnetic field B_{res} at R_i, with perturbation $\boldsymbol{\delta B} = (B_{\text{res}}/1000\,\hat{e}_{\perp,1}, 0\,\hat{e}_{\perp,2}, 0\,\hat{e}_\parallel)$ and $k = 0$.

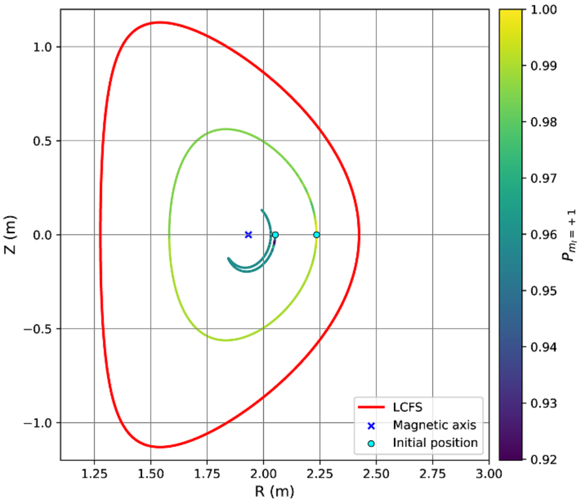

Figure 19. Trajectories of a trapped (banana) and passing (circular) deuteron in SPARC, showing the evolution over 10^4 cyclotron periods for particles initialized in the $m_I = +1$ spin state. The color indicates the instantaneous probability of being in the $m_I = +1$ spin state. The trapped particle is launched at $R = 2.052$ m with $E_\parallel = 900$ eV, $E_\perp = 8000$ eV, and the passing particle at $R = 2.235$ m with $E_\parallel = 3000$ eV, $E_\perp = 3000$ eV.

of occupying the $m_I = +1$ spin state, obtained using the same simulation setup described in this paragraph.

The analysis across four flux surfaces in SPARC (see figure 18) shows that depolarization is most pronounced in the trapped region of phase space (low $E_{\|}$, high $E_{\perp}$) and becomes more significant at larger radii, where the trapped-particle fraction increases. Passing particles show the strongest and most scattered depolarization near the core, but as the radius increases, the spread decreases and the probabilities cluster at higher values. Overall, orbit topology (trapped vs. passing) rather than total energy is the dominant factor for depolarization, and it is favorable that the trapped fraction remains small in the core where fusion reactions predominantly occur; however, a fraction of passing particles near the core are more prone to depolarization.

These results can be explained by noting that the cumulative spin depolarization depends on the relative time particles spend in resonance versus off resonance: extended time in resonance enhances depolarization, while longer recovery periods off resonance mitigate it and help restore polarization. Differences in orbit geometry between trapped and passing particles affect the relative time spent in and out of resonance, making trapped particles generally more prone to depolarization. A fraction of passing particles near the core, confined to smaller-radius flux surfaces, exhibit stronger depolarization, whereas those on larger-radius flux surfaces depolarize less, as their extended trajectories reduce the relative time spent in resonance and increase time in non-resonant regions.

9. Discussion

In this work we have shown a comprehensive numerical investigation of spin depolarization due to waves in plasma with frequencies comparable to the ion-cyclotron frequency. In particular, we focused on calculating depolarization in the SPARC tokamak at different radial locations and across deuterium and tritium energies in the presence of powerful spin-resonant shear eigenmode-like magnetic field perturbations. Overall, we have found the depolarization is weak over tens of thousands of ion cyclotron periods. While further work is required to study the evolution over longer time periods, these results suggest that spin-polarized deuterium and tritium could persist for sufficiently long enough to increase power density in magnetic confinement fusion machines.

To conduct this study, we developed a tool capable of self-consistently integrating the position, velocity, and particle spin state of ions in a superposition of a static uniform magnetic field and an arbitrary number of spatially and temporally oscillating magnetic fields. Using this framework, we identified normal modes supported by an infinite homogeneous D–T plasma with the potential to depolarize deuterium based on their degree of left-handed circular polarization and frequency. Our analysis shows that waves on the ion–ion hybrid branch may drive deuterium depolarization, while parallel-propagating waves on the fast Alfvén branch may similarly affect tritium.

We studied the role of alpha-particle birth distributions arising from SPF schemes, evaluating their ability to destabilize waves in a manner analogous to calculations performed for ICE. These distributions are found to emit waves obliquely to the magnetic field and only 20% larger than alpha-particle shell distributions generated from unpolarized fuel. Fully nonlinear electromagnetic PIC simulations revealed the relative strength of obliquely propagating Alfvén waves and showed that they represent the dominant risk to spin polarization. Compared to zero parallel wavenumber, a small but finite value amplifies relative magnetic fluctuation amplitudes by two to three orders of magnitude and drives strong left-handed polarization near the D and T precession frequencies. Notably, the choice of fuel polarization scheme does not alter wave magnitude or polarization, while increasing the alpha fraction raises the mean magnetic fluctuation amplitude without changing its polarization characteristics.

Monte Carlo integration was used to evaluate the spatio-temporal expectation value of the deuterium fuel polarization state in SPARC-like equilibria. These calculations indicate that depolarization remains modest even on collisional timescales for both deuterium and tritium when subjected to powerful waves near their respective precession frequencies.Finally, we highlight that high magnetic field strength could provide an intrinsic advantage for preserving spin alignment. Since the efficacy of depolarization depends on the relative perturbation $\delta B/B$ rather than the absolute amplitude δB, operation at higher B naturally suppresses this ratio if δB remains constant, offering an important mechanism to sustain polarization in next-generation high-field devices.

Acknowledgments

We acknowledge funding from Stellar Energy Foundation. We are grateful for conversations with R W Engels, W W Heidbrink, A Rutkowski, and J A Schwartz. We acknowledge the computational resources of the Flux HPC cluster at the Princeton Plasma Physics Laboratory used in this research work.

Appendix. ITER results

The PIC simulation results for ITER (figures 20–22) reproduce the SPARC trends: oblique magnetic field angles (small finite $k_{\|}$) amplify magnetic fluctuations and drive a transition toward left-handed polarization. The fluctuation amplitude increases with the fast-alpha fraction, yet is largely insensitive to the chosen fuel-polarization scheme. The Stokes ratio S_3/S_0 is independent of both the alpha fraction and the fuel polarization.

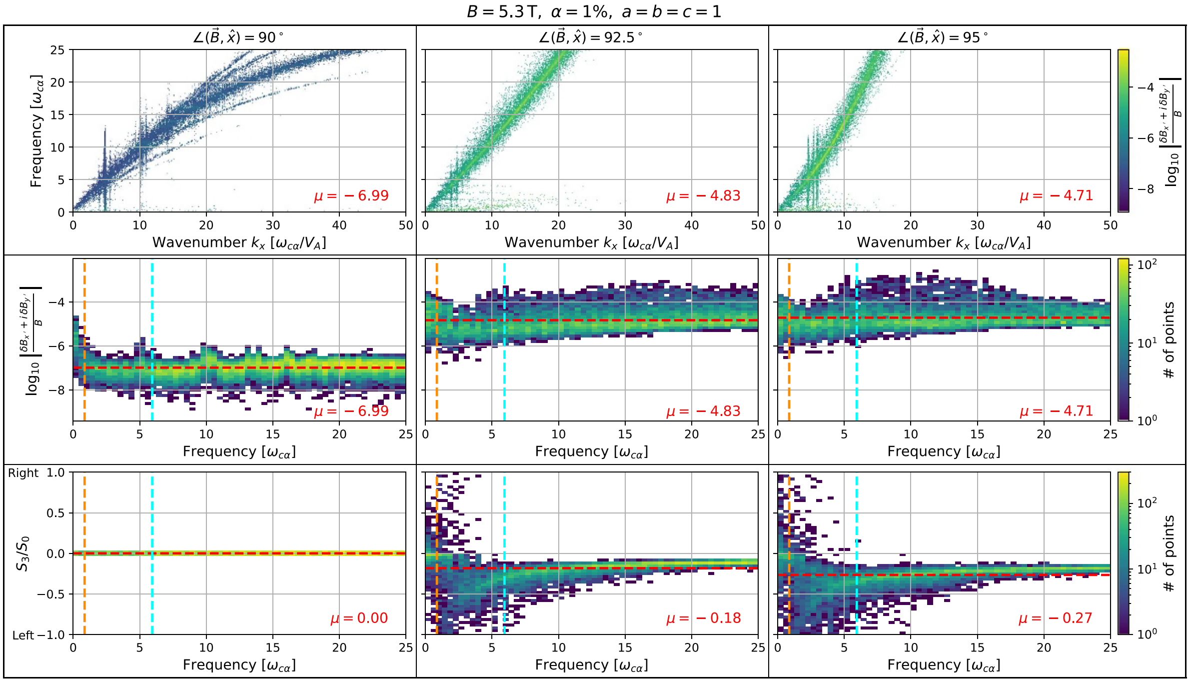

Figure 20. EPOCH simulation results for ITER at three magnetic field orientations relative to the simulation domain ($\angle(\vec{B},\hat{x}) = 90^\circ$, 92.5°, 95°, shown column-wise), with constant alpha fraction ($\alpha = 1\%$) and fuel polarization ($a = b = c = 1$).

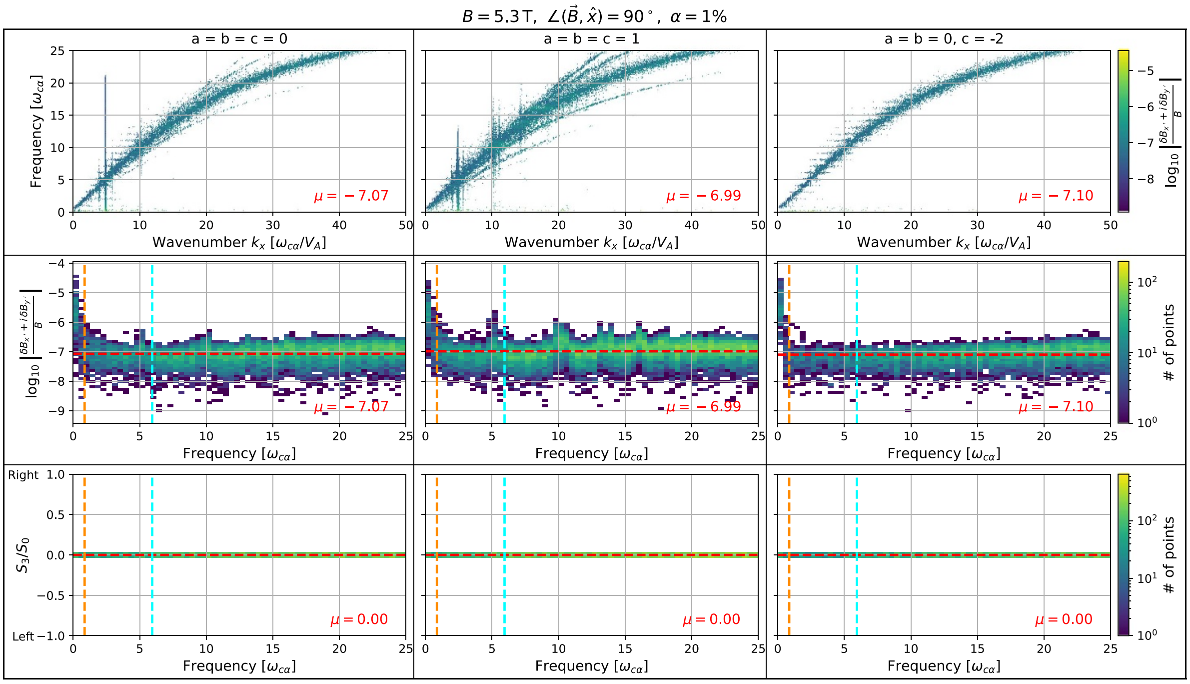

Figure 21. EPOCH simulation results for ITER at three fuel polarization configurations ($a = b = c = 0$, $a = b = c = 1$, and $a = b = 0$, $c = -2$, shown column-wise), with constant magnetic field orientation $\angle(\vec{B},\hat{x}) = 90^\circ$, and alpha fraction $\alpha = 1\%$.

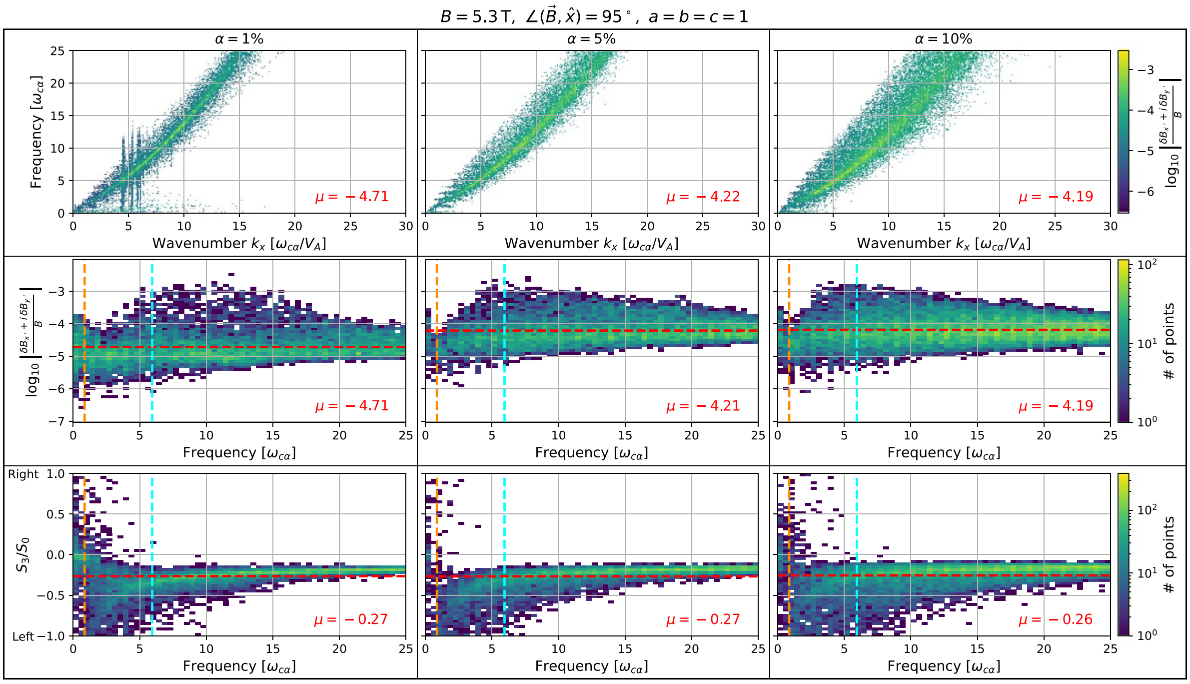

Figure 22. EPOCH simulation results for ITER at three alpha fractions ($\alpha = 1\%$, 5%, 10%, shown column-wise), with constant magnetic field orientation $\angle(\vec{B},\hat{x}) = 95^\circ$, and fuel polarization $a = b = c = 1$.

ORCID iDs

J.W.S. Cook 0000-0002-1905-5218
H. Ali 0000-0001-9649-3396
J.F. Parisi 0000-0003-1328-7154
A. Diallo 0000-0002-0706-060X
N. Faatz 0000-0003-0725-9253

References

[1] Abdou M.A. (the APEX Team) 1999 Exploring novel high power density concepts for attractive fusion systems *Fusion Eng. Des.* **45** 145

[2] Wade M.R. and Leuer J.A. 2021 Cost drivers for a tokamak-based compact pilot plant *Fusion Sci. Technol.* **77** 119

[3] Lawson J.D. 1957 Some criteria for a power producing thermonuclear reactor *Proc. Phys. Soc. B* **70** 6

[4] Keilhacker M. *et al* 1999 High fusion performance from deuterium-tritium plasmas in JET *Nucl. Fusion* **39** 209

[5] Creely A.J. *et al* 2020 Overview of the sparc tokamak *J. Plasma Phys.* **86** 865860502

[6] Wurzel S.E. and Hsu S.C. 2022 Progress toward fusion energy breakeven and gain as measured against the Lawson criterion *Phys. Plasmas* **29** 062103

[7] Austin M.E. *et al* 2019 Achievement of reactor-relevant performance in negative triangularity shape in the DIII-D tokamak *Phys. Rev. Lett.* **122** 115001

[8] Parisi J. *et al* 2025 Doubling fusion power with volumetric optimization in magnetic confinement fusion devices *Phys. Rev. Res.* **7** 013139

[9] Kulsrud R., Furth H., Valeo E. and Goldhaber M. 1982 Fusion reactor plasmas with polarized nuclei *Phys. Rev. Lett.* **49** 1248

[10] Cowley S., Kulsrud R. and Valeo E. 1984 Kinetic equation for spin-polarized plasmas *Technical Report* (Princeton Plasma Physics Laboratory)

[11] Kulsrud R.M., Valeo E.J. and Cowley S.C. 1986 Physics of spin-polarized plasmas *Nucl. Fusion* **26** 1443–62

[12] Sandorfi A. *et al* 2017 Polarized fusion, its implications and plans for direct measurements in a tokamak (arXiv:1703.06165)

[13] Heidbrink W.W., Baylor L.R., Bü,scher M., Engels R.W., Garcia A.V., Ghiozzi A.G., Miller G.W., Sandorfi A.M. and Wei X. 2024 A research program to measure the lifetime of spin polarized fuel *Front. Phys.* **12** 1355212

[14] More R.M. 1983 Nuclear spin-polarized fuel in inertial fusion *Phys. Rev. Lett.* **51** 396–9

[15] Mitarai O., Hasuyama H. and Wakuta Y. 1992 Spin polarization effect on ignition access condition for D-T and D-^{3}He tokamak fusion reactors *Fusion Technol.* **21** 2265–83

[16] Temporal M., Brandon V., Canaud B., Didelez J.P., Fedosejevs R. and Ramis R. 2012 Ignition conditions for inertial confinement fusion targets with a nuclear spin-polarized DT fuel *Nucl. Fusion* **52** 103011

[17] Ciullo G. *et al* 2016 *Nuclear Fusion With Polarized Fuel* vol 187 (Springer)

[18] Smith S. *et al* 2018 The potential for retention of spin polarization to raise fusion reactivity *27th IAEA Fusion Energy Conf. [FIP/P3-10]* (*Gandhinagar, India, 22–27 October 2018*) (available at: https://nucleus.iaea.org/sites/fusionportal/SharedDocuments/FEC2018/fec2018-preprints/preprint0290.pdf)

[19] Parisi J. and Diallo A. 2025 Electric power enhancement using spin-polarized fuel in fusion power plants (arXiv:2502.15941)

[20] Troyon F., Gruber R., Saurenmann H., Semenzato S. and Succi S. 1984 MHD-limits to plasma confinement *Plasma Phys. Control. Fusion* **26** 209

[21] Greenwald M., Terry J.L., Wolfe S.M., Ejima S., Bell M.G., Kaye S.M. and Neilson G.H. 1988 A new look at density limits in tokamaks *Nucl. Fusion* **28** 2199

[22] Horton W. 1999 Drift waves and transport *Rev. Mod. Phys.* **71** 735

[23] Jenko F., Dorland W. and Hammett G.W. 2001 Critical gradient formula for toroidal electron temperature gradient modes *Phys. Plasmas* **8** 4096

[24] Baker D.R. *et al* 2001 Thermal diffusivities in DIII-D show evidence of critical gradients *Phys. Plasmas* **8** 4128

[25] Ryter F., Angioni C., Peeters A.G., Leuterer F., Fahrbach H. and Suttrop W. 2005 Experimental study of trapped-electron-mode properties in tokamaks: threshold and stabilization by collisions *Phys. Rev. Lett.* **95** 085001

[26] Camenen Y. *et al* 2005 Electron heat transport in shaped TCV L-mode plasmas *Plasma Phys. Control. Fusion* **47** 1971

[27] Hender T. *et al* 2007 MHD stability, operational limits and disruptions *Nucl. Fusion* **47** S128

[28] Mantica P. *et al* 2009 Experimental study of the ion critical-gradient length and stiffness level and the impact of rotation in the JET tokamak *Phys. Rev. Lett.* **102** 175002

[29] Hillesheim J. *et al* 2013 Observation of a critical gradient threshold for electron temperature fluctuations in the DIII-D tokamak *Phys. Rev. Lett.* **110** 045003

[30] Stober J. *et al* 2000 Effects of triangularity on confinement, density limit and profile stiffness of H-modes on ASDEX Upgrade *Plasma Phys. Control. Fusion* **42** A211

[31] Garbet X. *et al* 2004 Profile stiffness and global confinement *Plasma Phys. Control. Fusion* **46** 1351

[32] Holland C. *et al* 2013 Validation studies of gyrofluid and gyrokinetic predictions of transport and turbulence stiffness using the DIII-D tokamak *Nucl. Fusion* **53** 083027

[33] Citrin J. *et al* 2014 Ion temperature profile stiffness: non-linear gyrokinetic simulations and comparison with experiment *Nucl. Fusion* **54** 023008

[34] Kim P. *et al* 2024 Optimization of nonlinear turbulence in stellarators *J. Plasma Phys.* **90** 905900210

[35] Parisi J. 2025 Introduction to stability and turbulent transport in magnetic confinement fusion plasmas (arXiv:2507.13144)

[36] Abdou M., Riva M., Ying A., Day C., Loarte A., Baylor L.R., Humrickhouse P., Fuerst T.F. and Cho S. 2021 Physics and technology considerations for the deuterium-tritium fuel cycle and conditions for tritium fuel self sufficiency *Nucl. Fusion* **61** 013001

[37] Meschini S., Ferry S.E., Delaporte-Mathurin R. and Whyte D.G. 2023 Modeling and analysis of the tritium fuel cycle for ARC- and STEP-class D-T fusion power plants *Nucl. Fusion* **63** 126005

[38] Parisi J., Diallo A. and Schwartz J. 2024 Simultaneous enhancement of tritium burn efficiency and fusion power with low-tritium spin-polarized fuel *Nucl. Fusion* **64** 126019

[39] Baylor L. *et al* 2023 Polarized fusion and potential in situ tests of fuel polarization survival in a tokamak plasma *Nucl. Fusion* **63** 076009

[40] Garcia A.V., Heidbrink W.W. and Sandorfi A.M. 2023 Conceptual design of DIII-D experiments to diagnose the lifetime of spin polarized fuel *Nucl. Fusion* **63** 026030

[41] Garcia A., Heidbrink W. and Sandorfi A. 2025 The use of D–D reactions to diagnose the lifetime of spin polarized fuel *Nucl. Fusion* **65** 046005

[42] Whan Bae J., Borowiec K., Badalassi V., Parisi J., Diallo A., Menard J., Khodak A. and Brown T. 2025 Neutronics analysis of spin-polarized fuel in spherical tokamaks *Nucl. Fusion* **65** 086051

[43] Rutkowski A., Harter J. and Parisi J. 2025 Scalable chrysopoeia via $(n, 2n)$ reactions driven by deuterium-tritium fusion neutrons (arXiv:2507.13461 [physics.plasm-ph])

[44] Parisi J., Diallo A. and Meschini S. 2025 Revisiting fusion in D-^{3}He plasmas with spin-polarized fuel (arXiv:2504.09869)

[45] Spiliotis A.K., Xygkis M., Koutrakis M.E., Tazes K., Boulogiannis G.K., Kannis C.S., Katsoprinakis G.E., Sofikitis D. and Rakitzis T.P. 2021 Ultrahigh-density spin-polarized hydrogen isotopes from the photodissociation of hydrogen halides: new applications for laser-ion acceleration, magnetometry and polarized nuclear fusion *Light: Sci. Appl.* **10** 35

[46] Reichwein L., Gong Z., Zheng C., Ji L.L., Pukhov A. and Büscher M. 2025 Plasma acceleration of polarized particle beams *Rep. Prog. Phys.* **88** 117001

[47] Kannis C. and Rakitzis T. 2025 Production of spin-polarized molecular beams via microwave or infrared rotational excitation (arXiv:2503.08435)

[48] Zheng C. *et al* 2024 Preservation of ^{3}He ion polarization after laser-plasma acceleration (arXiv:2310.04184 [physics.plasm-ph])

[49] Coppi B., Pegoraro F. and Ramos J. 1983 Instability of fusing plasmas and spin-depolarization processes *Phys. Rev. Lett.* **51** 892

[50] Goel B. and Heeringa W. 1988 Spin polarized ICF targets *Nucl. Fusion* **28** 355

[51] Kulsrud R. 2010 Polarization of P B11 in the FRC *Technical Report* (TAE Technologies)

[52] Paetz gen. Schieck H. 2016 Spin physics and polarized fusion: Where we stand *Nuclear Fusion With Polarized Fuel* (Springer) pp 15–34

[53] Gatto R. 2016 Depolarization of magnetically confined plasmas *Nuclear Fusion With Polarized Fuel* (Springer) pp 79–105

[54] Buttery R. *et al* 2019 DIII-D research to prepare for steady state advanced tokamak power plants *J. Fusion Energy* **38** 72

[55] Hu R., Zhou H., Tao Z., Lv M., Zou S. and Ding Y. 2020 Spin depolarization induced by self-generated magnetic fields during cylindrical implosions *Phys. Rev. E* **102** 043215

[56] Hu R., Zhou H., Tao Z., Zhang Z., Lv M., Zou S. and Ding Y. 2023 Numerical study of spin-polarized deuterium-tritium fuel persistence in inertial confinement fusion implosions *Phys. Rev. Res.* **5** 033115

[57] Eckstein W., Matschke F. and Verbeek H. 1976 Reflection of hydrogen from stainless steel and Nb *J. Nucl. Mater.* **63** 199

[58] Greenside H., Budny R. and Post D.E. 1984 Depolarization of D–T plasmas by recycling in material walls *J. Vac. Sci. Technol. A* **2** 619

[59] Wu Z. 2021 Wall interactions of spin-polarized atoms *Rev. Mod. Phys.* **93** 035006

[60] Causey R.A. 2002 Hydrogen isotope retention and recycling in fusion reactor plasma-facing components *J. Nucl. Mater.* **300** 91

[61] Majeski R., Doerner R., Gray T., Kaita R., Maingi R., Mansfield D., Spaleta J., Soukhanovskii V., Timberlake f. J. and Zakharov L. 2006 Enhanced energy confinement and performance in a low-recycling tokamak *Phys. Rev. Lett.* **97** 075002

[62] Zakharov L., Blanchard W., Kaita R., Kugel H., Majeski R. and Timberlake J. 2007 Low recycling regime in ITER and the LiWall concept for its divertor *J. Nucl. Mater.* **363** 453

[63] Douai D. *et al* 2015 Wall conditioning for ITER: current experimental and modeling activities *J. Nucl. Mater.* **463** 150

[64] Maan A. *et al* 2024 Estimates of global recycling coefficients for LTX-β discharges *Phys. Plasmas* **31** 022505

[65] Lodder J. 1983 On the possibility of nuclear spin polarization in fusion reactor plasmas *Phys. Lett. A* **98** 179

[66] Coppi B., Cowley S., Detragiache P., Kulsrud R. and Pegoraro F. 1986 High energy components and collective modes in thermonuclear plasmas *Technical Report* (Princeton Plasma Physics Laboratory)

[67] Davidson R. and Ogden J.M. 1975 Electromagnetic ion cyclotron instability driven by ion energy anisotropy in high-beta plasmas *Phys. Fluids* **18** 1045

[68] Dendy R., Lashmore-Davies C., McClements K.G. and Cottrell G. 1994 The excitation of obliquely propagating fast Alfvén waves at fusion ion cyclotron harmonics *Phys. Plasmas* **1** 1918

[69] Gorelenkov N. and Cheng C. 1995 Alfven cyclotron instability and ion cyclotron emission *Nucl. Fusion* **35** 1743

[70] Fasoli A. *et al* 1997 Alfvén eigenmode experiments in tokamaks and stellarators *Plasma Phys. Control. Fusion* **39** B287

[71] Brambilla M. 1999 Numerical simulation of ion cyclotron waves in tokamak plasmas *Plasma Phys. Control. Fusion* **41** 1

[72] Heidbrink W. 2008 Basic physics of Alfvén instabilities driven by energetic particles in toroidally confined plasmas *Phys. Plasmas* **15** 055501

[73] Cramer N.F. 2011 *The Physics of Alfvén Waves* (Wiley)

[74] Garcia-Munoz M. *et al* 2011 Fast-ion transport induced by Alfvén eigenmodes in the ASDEX Upgrade tokamak *Nucl. Fusion* **51** 103013

[75] Dendy R. and McClements K. 2015 Ion cyclotron emission from fusion-born ions in large tokamak plasmas: a brief review from JET and TFTR to ITER *Plasma Phys. Control. Fusion* **57** 044002

[76] Chen L. and Zonca F. 2016 Physics of Alfvén waves and energetic particles in burning plasmas *Rev. Mod. Phys.* **88** 015008

[77] Prokopyszyn A., Mcclements K., Oliver H., Fitzgerald M., Ryan D. and Xia G. 2025 Confinement of fusion alpha-particles and Alfven eigenmode stability in STEP *Nucl. Fusion* **65** 086039

[78] Kolesnichenko Y., Fülöp T., Lisak M. and Anderson D. 1998 Localized fast magnetoacoustic eigenmodes in tokamak plasmas *Nucl. Fusion* **38** 1871

[79] Fülöp T., Lisak M., Kolesnichenko Y.I. and Anderson D. 2000 The radial and poloidal localization of fast magnetoacoustic eigenmodes in tokamaks *Phys. Plasmas* **7** 1479

[80] Smith H., Fülöp T., Lisak M. and Anderson D. 2003 Localization of compressional Alfven eigenmodes in spherical tori *Phys. Plasmas* **10** 1437

[81] Belikov V.S. and Kolesnichenko Y.I. 1976 Magnetoacoustic cyclotron instability in a thermonuclear plasma *Sov. Phys. Tech. Phys.* **20** 1146

[82] Dendy R.O., Lashmore-Davies C.N. and Kam K.F. 1992 A possible excitation mechanism for observed superthermal ion cyclotron emission from tokamak plasmas *Phys. Fluids B* **4** 3996

[83] Dendy R.O., Lashmore-Davies C.N. and Kam K.F. 1993 The magnetoacoustic cyclotron instability of an extended shell distribution of energetic ions *Phys. Fluids B* **5** 1937

[84] Cook J.W.S. 2022 Doublet splitting of fusion alpha particle driven ion cyclotron emission *Plasma Phys. Control. Fusion* **64** 115002

[85] TFR E. 1978 High-power neutral injection and ion power balance in TFR *Nucl. Fusion* **18** 1271

[86] Cottrell G.A. and Dendy R.O. 1988 Superthermal radiation from fusion products in JET *Phys. Rev. Lett.* **60** 33

[87] Cottrell G.A., Bhatnagar V.P., Da Costa O., Dendy R.O., Jacquinot J., McClements K.G., McCune D.C., Nave M.F.F., Smeulders P. and Start D.F.H. 1993 Ion cyclotron emission measurements during JET deuterium-tritium experiments *Nucl. Fusion* **33** 1365

[88] McClements K.G., Hunt C., Dendy R.O. and Cottrell G.A. 1999 Ion cyclotron emission from JET DT plasmas *Phys. Rev. Lett.* **82** 2099

[89] Cottrell G.A. 2000 Identification of minority ion-cyclotron emission during radio frequency heating in the JET tokamak *Phys. Rev. Lett.* **84** 2397

[90] Jacquet P. *et al* 2011 Parasitic signals in the receiving band of the sub-harmonic arc detection system on JET ICRF antennas *AIP Conf. Proc.* **1406** 17–20

[91] McClements K.G., Brisset A., Chapman B., Chapman S.C., Dendy R.O., Jacquet P., Kiptily V.G., Mantsinen M. and Reman B.C. (JET Contributors) 2018 Observations and modelling of ion cyclotron emission observed in JET plasmas using a sub-harmonic arc detection system during ion cyclotron resonance heating *Nucl. Fusion* **58** 096020

[92] Cauffman S., Majeski R., McClements K.G. and Dendy R.O. 1995 Alfvénic behaviour of alpha particle driven ion cyclotron emission in TFTR *Nucl. Fusion* **35** 1597

[93] Dendy R.O., McClements K.G., Lashmore-Davies C.N., Cottrell G.A., Majeski R. and Cauffman S. 1995 Ion cyclotron emission due to collective instability of fusion products and beam ions in TFTR and JET *Nucl. Fusion* **35** 1733

[94] Cauffman S. and Majeski R. 1995 Ion cyclotron emission on the tokamak fusion test reactor *Rev. Sci. Instrum.* **66** 817

[95] D'Inca R. 2014 Ion cyclotron emission on ASDEX Upgrade *PhD Thesis* Ludwig Maximillian University

[96] Ochoukov R. *et al* 2018 Core plasma ion cyclotron emission driven by fusion-born ions *Nucl. Fusion* **59** 014001

[97] Ochoukov R. *et al* 2018 Observations of core ion cyclotron emission on ASDEX Upgrade tokamak *Rev. Sci. Instrum.* **89** 10J101

[98] Askinazi L.G., Belokurov A.A., Gin D.B., Kornev V.A., Lebedev S.V., Shevelev A.E., Tukachinsky A.S. and Zhubr N.A. 2018 Ion cyclotron emission in NBI-heated plasmas in the TUMAN-3M tokamak *Nucl. Fusion* **58** 082003

[99] Askinazi L. *et al* 2018 The spectrum of ion cyclotron emission from neutral beam injection heated plasma on the TUMAN-3M tokamak *Tech. Phys. Lett.* **44** 1020

[100] Thome K.E., Pace D.C., Pinsker R.I., Van Zeeland M.A., Heidbrink W.W. and Austin M.E. 2019 Central ion cyclotron emission in the DIII-D tokamak *Nucl. Fusion* **59** 086011

[101] DeGrandchamp G.H., Lestz J.B., Van Zeeland M.A., Du X.D., Heidbrink W.W., Thome K.E., Crocker N.A. and Pinsker R.I. 2022 Mode structure measurements of ion cyclotron emission and sub-cyclotron modes on DIII-D *Nucl. Fusion* **62** 106033

[102] Crocker N. *et al* 2022 Novel internal measurements of ion cyclotron frequency range fast-ion driven modes *Nucl. Fusion* **62** 026023

[103] Liu L.N. *et al* 2019 Ion cyclotron emission diagnostic system on the Experimental Advanced Superconducting Tokamak and first detection of energetic-particle-driven radiation *Rev. Sci. Instrum.* **90** 063504

[104] Liu L. *et al* 2020 Ion cyclotron emission driven by deuterium neutral beam injection and core fusion reaction ions in EAST *Nucl. Fusion* **60** 044002

[105] Tong R. *et al* 2022 Development of the ion cyclotron emission diagnostic on the HL-2A tokamak *J. Instrum.* **17** C01063

[106] Liu L. *et al* 2023 Identification of core ion cyclotron instabilities on HL-2A tokamak *Nucl. Fusion* **63** 104004

[107] Kimura H. *et al* 1998 Alfvén eigenmode and energetic particle research in JT-60U *Nucl. Fusion* **38** 1303

[108] Ichimura M., Higaki H., Kakimoto S., Yamaguchi Y., Nemoto K., Katano M., Ishikawa M., Moriyama S. and Suzuki T. 2008 Observation of spontaneously excited waves in the ion cyclotron frequency range on JT-60U *Nucl. Fusion* **48** 035012

[109] Ichimura M. *et al* 2008 Study of ion cyclotron emissions due to DD fusion product ions on JT-60U *22nd IAEA Fusion Energy Conf.* (*Geneva, Switzerland*, *13–18 October 2008*) pp EX–8

[110] Sato S. *et al* 2010 Observation of ion cyclotron emission owing to DD fusion product h ions in JT-60U *Plasma Fusion Res.* **5** S2067

[111] Sumida S., Shinohara K., Ikezoe R., Ichimura M., Sakamoto M., Hirata M. and Ide S. 2017 Comparison of dispersion model of magneto-acoustic cyclotron instability with experimental observation of ^{3}He ion cyclotron emission on JT-60U *J. Phys. Soc. Japan* **86** 124501

[112] Sumida S., Shinohara K., Ikezoe R., Ichimura M., Sakamoto M., Hirata M. and Ide S. 2019 Characteristics of fast ^{3}He ion velocity distribution exciting ion cyclotron emission on JT-60U *Plasma Phys. Control. Fusion* **61** 025014

[113] Kim M.H., Thatipamula S.G., Lee J.E., Choi M.J., Park H.K., Akiyama T. and Yun G.S. 2018 Distinct stages of radio frequency emission at the onset of pedestal collapse in KSTAR H-mode plasmas *Nucl. Fusion* **58** 096034

[114] Thatipamula S.G., Yun G.S., Leem J., Park H.K., Kim K.W., Akiyama T. and Lee S.G. 2016 Dynamic spectra of radio frequency bursts associated with edge-localized modes *Plasma Phys. Control. Fusion* **58** 065003

[115] Fredrickson E.D., Gorelenkov N.N., Bell R.E., Diallo A., LeBlanc B.P. and Podestà M. 2019 Emission in the ion cyclotron range of frequencies (ICE) on NSTX and NSTX-U *Phys. Plasmas* **26** 032111

[116] Fredrickson E. *et al* 2021 Chirping ion cyclotron emission (ICE) on NSTX-U *Nucl. Fusion* **61** 086007

[117] Saito K. *et al* 2009 Measurement of ion cyclotron emissions by use of ICRF heating antennas in LHD *Fusion Eng. Des.* **84** 1676

[118] Saito K. *et al* 2013 Measurement of ion cyclotron emissions by using high-frequency magnetic probes in the LHD *Plasma Sci. Technol.* **15** 209

[119] Shalashov A., Suvorov E.V., Lubyako L.V. and Maassberg H. (the W7-AS Team) 2003 NBI-driven ion cyclotron instabilities at the W7-AS stellarator *Plasma Phys. Control. Fusion* **45** 395

[120] Moseev D. *et al* 2021 Development of the ion cyclotron emission diagnostic for the W7-X stellarator *Rev. Sci. Instrum.* **92** 033546

[121] Samant O., Dendy R., Chapman S., Tripathi S., Carter T., Van Compernolle B. and Cook J. 2025 Physics of beam-driven ion cyclotron emission in the large plasma device *Nucl. Fusion* **65** 066023

[122] Chapman B., Dendy R.O., Chapman S.C., Holland L.A., Irvine S.W.A. and Reman B.C.G. 2020 Comparing theory and simulation of ion cyclotron emission from energetic ion populations with spherical shell and ring-beam distributions in velocity-space *Plasma Phys. Control. Fusion* **62** 055003

[123] Ochoukov R. *et al* 2019 Interpretation of core ion cyclotron emission driven by sub-Alfvénic beam-injected ions via magnetoacoustic cyclotron instability *Nucl. Fusion* **59** 086032

[124] Pan Y. and Hatchett S. 1987 Spin-polarized fuel in high gain ICF targets *Nucl. Fusion* **27** 815

[125] Allen L. and Eberly J.H. 2012 *Optical Resonance and Two-Level Atoms* (Courier Corporation)

[126] Pauli W. 1927 Zur Quantenmechanik des magnetischen elektrons *Z. Phys.* **43** 601

[127] Magnus W. 1954 On the exponential solution of differential equations for a linear operator *Commun. Pure Appl. Math.* **7** 649

[128] Verner J.H. 2007 A “more efficient” Runge–Kutta (9)8 pair with interpolants *Technical Report* (Simon Fraser University)

[129] Rabi I.I. 1937 Space quantization in a gyrating magnetic field *Phys. Rev.* **51** 652

[130] Stix T.H. 1992 *The Theory of Plasma Waves* (AIP Press)

[131] Brambilla M. 1998 *Kinetic Theory of Plasma Waves: Homogeneous Plasmas* (Oxford University Press)

[132] Swanson D.G. 2003 *Plasma Physics for Physicists and Engineers* (CRC Press)

[133] Slade-Harajda T.W., Cook J.W.S., Dendy R.O. and Chapman S.C. 2025 Effects of deuterium-tritium mix on linear growth rates of the magnetoacoustic cyclotron instability in fusion plasmas *Phys. Plasmas* **32** 082506

[134] Lerche I. 1966 Transverse waves in a relativistic plasma *Phys. Fluids* **9** 1073

[135] Newberger B.S. 1982 New sum rule for products of Bessel functions with application to plasma physics *J. Math. Phys.* **23** 1278

[136] Chapman B., Dendy R.O., Chapman S.C., McClements K.G. and Ochoukov R. 2020 Origin of ion cyclotron emission at the proton cyclotron frequency from the core of deuterium plasmas in the ASDEX-Upgrade tokamak *Plasma Phys. Control. Fusion* **62** 095022

[137] Birdsall C.K. and Langdon A.B. 1985 *Plasma Physics Via Computer* (McGraw-Hill)

[138] Villasenor J. and Buneman O. 1992 Rigorous charge conservation for local electromagnetic field solvers *Comput. Phys. Commun.* **69** 306

[139] Cook J.W.S., Dendy R.O. and Chapman S.C. 2013 Particle-in-cell simulations of the magnetoacoustic cyclotron instability of fusion-born alpha-particles in tokamak plasmas *Plasma Phys. Control. Fusion* **55** 065003

[140] Toida M., Saito K., Igami H., Akiyama T., Kamio S. and Seki R. 2018 Simulation study of high-frequency magnetosonic waves excited by energetic ions in association with ion cyclotron emission *Plasma Fusion Res.* **13** 3403015

[141] Chapman B., Dendy R.O., Chapman S.C., McClements K.G., Yun G.S., Thatipamula S.G. and Kim M.H. 2019 Interpretation of suprathermal emission at deuteron cyclotron harmonics from deuterium plasmas heated by neutral beam injection in the KSTAR tokamak *Nucl. Fusion* **59** 106021

[142] Reman B.C.G., Dendy R.O., Akiyama T., Chapman S.C., Cook J.W.S., Igami H., Inagaki S., Saito K. and Yun G.S. 2019 Interpreting observations of ion cyclotron emission from large helical device plasmas with beam-injected ion populations *Nucl. Fusion* **59** 096013

[143] Samant O., Dendy R.O., Chapman S.C., Moseev D. and Ochoukov R. 2024 Predicting ion cyclotron emission from neutral beam heated plasmas in Wendelstein7-X stellarator *Nucl. Fusion* **64** 056022

[144] Arber T.D. *et al* 2015 Contemporary particle-in-cell approach to laser-plasma modelling *Plasma Phys. Control. Fusion* **57** 1

[145] Hellsten T. and Laxaback M. 2003 Edge localized magnetosonic eigenmodes in the ion cyclotron frequency range *Phys. Plasmas* **10** 4371

[146] Smith H.M. and Verwichte E. 2009 Compressional Alfvén eigenmode structure in spherical tokamaks *Plasma Phys. Control. Fusion* **51** 075001

[147] Sharapov S.E. *et al* 2014 Bi-directional Alfvén cyclotron instabilities in the Mega-Amp Spherical Tokamak *Phys. Plasmas* **21** 082501

[148] Bradshaw J.C. 2020 Modelling of compressional Alfvén eigenmodes in axisymmetric toroidal fusion plasmas *PhD Thesis* University of Warwick (available at: https://wrap.warwick.ac.uk/id/eprint/161400/1/WRAP_Theses_Bradshaw_2020.pdf)